Kinetics of the Reaction of Methyl Radical with Hydroxyl Radical and Methanol Decomposition†

Ahren W. Jasper,* Stephen J. Klippenstein,* Lawrence B. Harding, and Branko Ruscic

Chemistry Division, Argonne National Laboratory, Argonne, Illinois 60439

Received: November 15, 2006; In Final Form: February 8, 2007

The $CH_3 + OH$ bimolecular reaction and the dissociation of methanol are studied theoretically at conditions relevant to combustion chemistry. Kinetics for the $CH_3 + OH$ barrierless association reaction and for the $H + CH_2OH$ and $H + CH_3O$ product channels are determined in the high-pressure limit using variable reaction coordinate transition state theory and multireference electronic structure calculations to evaluate the fragment interaction energies. The $CH_3 + OH \rightarrow {}^3CH_2 + H_2O$ abstraction reaction and the $H_2 + HCOH$ and $H_2 + H_2CO$ product channels feature localized dynamical bottlenecks and are treated using variational transition state theory and QCISD(T) energies extrapolated to the complete basis set limit. The $^1CH_2 + H_2O$ product channel has two dynamical regimes, featuring both an inner saddle point and an outer barrierless region, and it is shown that a microcanonical two-state model is necessary to properly describe the association rate for this reaction over a broad temperature range. Experimental channel energies for the methanol system are reevaluated using the Active Thermochemical Tables (ATcT) approach. Pressure dependent, phenomenological rate coefficients for the $CH_3 + OH$ bimolecular reaction and for methanol decomposition are determined via master equation simulations. The predicted results agree well with experimental results, including those from a companion high-temperature shock tube determination for the decomposition of methanol.

I. Introduction

For decades methanol has been identified as a promising alternative fuel,[1] and it has desirable properties as a gasoline additive.[2] In hydrocarbon flames, the formation of methanol can act as a sink for methyl and hydroxyl radicals, and the subsequent oxidation or thermal dissociation of methanol produces a variety of reactive radicals and molecules. Knowledge of the rates and product distributions associated with the formation and decomposition of methanol is therefore important for the development of combustion models of flame speed and heat release.

We first consider the bimolecular reaction

$$CH_3 + OH \rightarrow CH_3OH^* (+M) \rightarrow CH_3OH \quad (1a)$$

$$\rightarrow {}^1CH_2 + H_2O \quad (1b)$$

$$\rightarrow cis\text{-}HCOH + H_2 \quad (1c)$$

$$\rightarrow trans\text{-}HCOH + H_2 \quad (1d)$$

$$\rightarrow H_2CO + H_2 \quad (1e)$$

$$\rightarrow CH_2OH + H \quad (1f)$$

$$\rightarrow CH_3O + H \quad (1g)$$

where CH_3OH^* indicates an energized complex, and collisional stabilization (1a) competes with decomposition to the bimolecular products 1b−1g. At elevated temperatures, direct abstraction on the triplet surface,

$$CH_3 + OH \rightarrow {}^3CH_2 + H_2O \quad (1h)$$

is also possible.

Reaction 1 is a prototypical R + OH reaction, where R denotes a hydrocarbon radical, and it has been studied extensively both experimentally and theoretically. Much of the experimental work has been performed near room temperature and atmospheric pressure, and considerable uncertainties remain. There is some consensus[3−8] in the experimentally measured rate coefficient for reaction 1 at room temperature and atmospheric pressure ($(7-9) \times 10^{-11}$ cm^3 molecule^{-1} s^{-1}), as well as evidence[5−7] that 1 atm is close to the high-pressure limit at 298 K. However, room-temperature values for k_1^∞ larger by approximately a factor of 2 have also been reported.[9,10] Grotheer and co-workers[11−13] observed no temperature dependence in k_1^∞ up to 700 K, and Fagerström et al.[14] measured a slight increase in k_1^∞ from 298 to 373 K. In contrast, de Avillez Pereira et al.[6] found that k_1^∞ decreased with increasing temperature by a factor of 2 over the temperature range 298−710 K.

At higher temperatures, experimental determinations of k_1 are limited to three shock tube studies. Bott and Cohen[15] reported a value at 1200 K and 1 atm that is one-third of the best fit expression obtained by Krasnoperov and Michael[16] on the basis of their studies at 800−1200 and 1800−2400 K and at similar pressures. More recently and reported in a companion paper,[17] Srinivasan et al. measured k_1 over the temperature range 1100−1350 K and obtained values somewhat lower than the earlier value of Bott and Cohen.

In addition to uncertainties in the overall rate coefficient for reaction 1, there is also some ambiguity in the measured product branching fractions. Grotheer and co-workers[9,11] inferred from experiments at low pressures that channel 1b contributed no

† Part of the special issue "James A. Miller Festschrift".

* Corresponding authors. E-mail: sjk@anl.gov (S.J.K.).

10.1021/jp067585p CCC: $37.00
Published on Web 03/16/2007

more than 5% and 10% to the total rate at 300 and 410 K, respectively, and that stabilization (1a) was the dominant product channel at pressures as low as 0.2−7 Torr. These results are in qualitative disagreement with those of Deters et al.[7] and Fockenberg et al.,[18] who both observed mainly (∼90%) $CH_2 + H_2O$ (1b) at room temperature and low pressures. At 700 K, Grotheer et al.[12,13] estimated channel 1b to contribute as much as 38% to the total rate and observed significant formation of H_2 + products (1c−1e). This result is in good agreement with Fockenberg et al.,[18] who reported that channels 1b and 1a accounted for 46 ± 14% and 20 ± 7% of the total rate at 610 K, respectively, with the rest attributed to channels 1c−1e.

The thermal decomposition of methanol,

$$CH_3OH\ (+M) \rightarrow CH_3 + OH \quad (2a)$$

$$\rightarrow {}^1CH_2 + H_2O \quad (2b)$$

$$\rightarrow cis\text{−}HCOH + H_2 \quad (2c)$$

$$\rightarrow trans\text{−}HCOH + H_2 \quad (2d)$$

$$\rightarrow H_2CO + H_2 \quad (2e)$$

$$\rightarrow CH_2OH + H \quad (2f)$$

$$\rightarrow CH_3O + H \quad (2g)$$

has also been studied extensively, including the recent experimental study of Srinivasan et al.,[17] which was carried out in collaboration with the present theoretical study. At high temperatures (1400−2500 K) and low pressures (∼100−1000 Torr), several experimental determinations[16,17,19−22] of k_2 have been made in which channels other than 2a were not always explicitly considered. The experimental results are typically in good agreement with one another and have generally been taken to represent the low-pressure limit for this reaction. Falloff for reaction 2 has also been measured. The results of Tsuboi et al.,[23] who considered pressures up to 10 atm, agree well with those of Hidaka et al.[24] at 3 atm and are somewhat higher than those reported by Spindler and Wagner[25] for pressures up to 6 atm. In an earlier study, Bowman[26] reported a significantly lower set of values at 3 atm. Two experimental studies[27,28] at lower temperatures (900−1200 K) and at low pressures (200−760 Torr) have also appeared, and these results indicate that reaction 2 is in the falloff regime under these conditions.

Several groups[16,17,20−22,24,25] have measured or estimated the importance of the $CH_2OH + H$ product channel for reaction 2 and found that it contributed ∼10−30% to the total rate. In contrast, Dombrowsky et al.[20] suggested ${}^1CH_2 + H_2O$ as the second most important product (up to 20%), with the formation of $CH_2OH + H$ comprising less than 5% of the total rate.

Experimental determinations of the rates of reactions 1 and 2 are generally complicated by competing reactions (e.g., the self-reactions of OH and CH_3, etc.) and by uncertainties in the secondary chemistry, especially at high temperatures. The extraction of rates from experimental observables often requires a detailed model of the reaction mechanism, which in turn requires rate coefficients at the conditions of interest for each elementary process in the mechanism. For some elementary processes, these rate coefficients are unknown or are only poorly known. Sensitivity analyses are often used to quantify the effect of these ambiguities on the measured rates, but uncertainties may remain, making it a challenge to understand the source of experimental discrepancies in the literature. Because different experiments suffer to different extents from these secondary chemistry problems, it is difficult to immediately recognize which are the more direct experiments. Fortunately, a detailed analysis of the available experimental measurements for reactions 1 and 2 has recently been made,[8] and these recommended values will be emphasized throughout this Article.

High-pressure rate coefficients may be obtained unambiguously from theory, but the accuracy of the computed rates is limited by the accuracy of the potential energy surface and/or by the treatment of the transition state. For example, two recent theoretical predictions of k_1^∞ at room temperature (1.5×10^{-11} and 2.2×10^{-10} cm^3 molecule^{-1} s^{-1} in refs 29 and 30, respectively) differ by more than an order of magnitude, and neither prediction falls within the range of experimental results. Furthermore, the two theoretical treatments show qualitatively different temperature dependences, with both positive[30] and negative[29] temperature dependences predicted. An earlier theoretical study by Jordan et al.[31] predicted a value for k_1^∞ with a magnitude similar to that of ref 29 but with a positive temperature dependence.

Additional uncertainties may arise when modeling pressure dependence. Finite pressure rate coefficients and product branching fractions may be obtained using simple phenomenological models or by solving the appropriate master equation. Reactions 1 and 2 feature a single deep well, which simplifies somewhat the calculation of pressure dependent rate coefficients. However, due to the presence of several competing bimolecular products, the widely used Troe models[32−34] for pressure dependence may not be appropriate.[35,36] Several master equation simulations for reactions 1 and 2 have appeared previously.[5,6,18,29,31] Xia et al.[29] recently performed a detailed theoretical study of reaction 2. They computed the potential energy surface for methanol using a high-level electronic structure theory method (G2M) and included channels 2a−2g in their master equation simulations. Their predicted low-pressure limit rate coefficient for reaction 2 agrees well with the experimental results discussed above. At 1 atm, however, Xia et al.[29] predict significant pressure dependence and 2b to be the dominant product channel (∼55%), with channels 2a and 2c contributing ∼30% and ∼13%, respectively. These results appear to be in disagreement with the experimental consensus that channel 2a dominates under these conditions.

In this Article, reactions 1 and 2 are studied theoretically using high-level electronic structure methods coupled with variational transition state theory and master equation simulations. The goal of this work is to provide a consistent picture of the kinetics and to resolve some of the current uncertainties and ambiguities. The present theoretical treatment differs in several important aspects from previous work, as discussed next.

The energetics of small stable molecules, such as those participating in reactions 1 and 2, may be readily computed using a variety of well-validated electronic structure methods with estimated 2σ uncertainties of ∼1 kcal/mol or less, but these uncertainties may still be kinetically important. Furthermore, uncertainties for nonequilibrium geometries, such as saddle points and geometries along reaction paths, are likely to be larger, perhaps by a factor of 2. The present work includes an analysis of available experimental thermochemical data relevant to the methanol system using the Active Thermochemical Tables (ATcT) approach.[37−40] This analysis provides energies for the reactant and product channels of reactions 1 and 2 with small (typically, <0.1 kcal/mol) experimental uncertainties. The availability of accurate experimental data for the relative channel energies and the study of the effect of these revised values on

the overall kinetics of reactions 1 and 2 is one motivation for the present study.

Next, we consider the treatment of the transition state. Reactions with forward and reverse barriers and "tight" transition states are often accurately modeled using variational transition state theory[41] (TST) and the rigid rotor and harmonic oscillator approximations. Corrections for tunneling and anharmonicity can be included when these effects are expected to be important. In reactions 1 and 2, the H_2 product channels and the direct abstraction reaction (1h) feature finite barriers and localized transition state regions. The $CH_3 + OH$ channel and the two H channels, however, are barrierless. An accurate description of barrierless reactions, which are ubiquitous in the chemistry of radicals and therefore combustion chemistry, typically requires knowledge of a more global region of the potential energy surface. The treatment of barrierless reactions is therefore often more approximate than the treatment of reactions with barriers. In fact, difficulties in treating the barrierless transition states in reactions 1 and 2 have led a number of the modeling studies to use simple models[29,30] or empirical estimates[5,6,18,42] for the rate coefficients for these channels. Due to the importance of these channels in the overall kinetics, uncertainties in the treatment of the barrierless transition states could be a significant source of error in previous theoretical treatments.

Recently, a direct ab initio implementation of the variable reaction coordinate TST (VRC-TST) method[43−45] has been used to study barrierless radical−radical association reactions involving hydrogen and hydrocarbon fragments.[46,47] This scheme treats the interaction potential between the reacting fragments as fully dimensional and without neglecting anharmonicities or couplings, and the difficulties associated with developing analytic representations of multidimensional potential energy surfaces are avoided. In refs 46 and 47, it was shown that rate coefficients for hydrocarbon association reactions could be efficiently computed with estimated errors of less than ∼20% using the VRC-TST approach and evaluating the potential energy surface directly using multireference electronic structure methods and moderately sized reference spaces and basis sets. The use of the VRC-TST method to treat the barrierless channels in reactions 1 and 2 is a key aspect of the present work. We note that Jordan et al.[31] computed the rate coefficient for $CH_3 + OH$ using a treatment for the barrierless transition state that is similar to the one applied in the present work. The accuracy of their result, however, is limited by their use of an empirical potential energy function to describe the interaction energy and by their use of a more restrictive set of dividing surfaces than the set considered in the present work.

The formation of $^1CH_2 + H_2O$ is an important product channel for both reactions 1 and 2 and features a shallow van der Waals well and a saddle point with an energy below that of the isolated products. These features give rise to two dynamical regimes: one corresponding to a long-range barrierless region, which may be expected to control the overall rate at low temperatures, and the other corresponding to an inner, localized transition state, which may be expected to control the rate at high temperatures. A similar situation exists for the $OH + C_2H_4$ reaction, and it has recently been shown[48] that an accurate treatment of the overall rate coefficient in that case requires a coupled treatment of the microcanonical fluxes for the inner and outer transition states. In the present work, we report capture rates for the $^1CH_2 + H_2O$ reaction (k^{∞}_{-1b}) using such a unified statistical model.[49] In some previous analyses[18,42] of reactions 1 and 2, k^{∞}_{-1b} was set equal to the room-temperature experimental value and was assumed to be independent of temperature. In other analyses, the two transition state regions were considered separately,[29] or either the inner[6] or the outer[30] transition state region was neglected.

Pressure dependent kinetics for reactions 1 and 2 are modeled via master equation simulations. The energy transfer function is determined by fitting to available experimental falloff data for reaction 1, and the resulting magnitude and temperature dependence of the energy transfer function agrees well with previous master equation simulations for similar systems.

The paper is organized as follows. In section II, experimental thermochemical data are analyzed within the ATcT framework, and high-level ab initio calculations are performed to obtain a composite experimental/theoretical potential energy surface. In section III, details of the VRC-TST method, the two-state kinetics model for channel 1b, and the master equation simulations are discussed. High-pressure limit rate coefficients for each of the bimolecular channels are presented in section IV, where they are compared with experimental and previous theoretical results. Also reported in section IV are pressure dependent rate coefficients and product branching fractions for $CH_3 + OH$ bimolecular reaction and for methanol dissociation, and detailed comparisons with experimental and previous theoretical results are made. Conclusions are given in section V.

II. Potential Energy Surface

II.A. Active Thermochemical Tables. Channel energies for the methanol system were determined using the Active Thermochemical Tables (ATcT) approach. ATcT are a new paradigm of how to obtain accurate, reliable, and internally consistent thermochemical values by using all available knowledge,[37−40] thus overcoming the limitations that are deeply engrained in the traditional approach to thermochemistry. As opposed to the traditional sequential approach, ATcT derives its results from a Thermochemical Network (TN), which explicitly contains the available experimental and theoretical thermochemical interdependencies between various chemical species (aka thermochemically relevant determinations). The pertinent details of the ATcT approach are given elsewhere,[37] so we emphasize here that the knowledge content of the TN is maximized by applying an iterative statistical analysis of all available thermochemical interdependencies, which is in turn made possible by the existence of redundancies in the TN, such as competing measurements and computations, alternate TN paths, etc. The ATcT results for the channel energies for reactions 1 and 2 are summarized in Table 1 and are based on version 1.062 of the Core (Argonne) Thermochemical Network [C(A)TN],[37,40] which is growing on a daily basis and currently encompasses ∼800 chemical species containing H, O, C, N, and halogens, interlinked by ∼8000 thermochemically relevant determinations. A detailed discussion of the portion of C(A)TN that is relevant to the sequential dissociation energies of methanol will be given separately in a forthcoming paper.[50]

One particularly important quantity is the enthalpy of reaction 1b. This reaction is nearly thermoneutral, and theoretical predictions[29,51] for this value vary from endothermic to exothermic by a few kcal/mol. Due to uncertainties in the heat of formation of $^1CH_2$, the experimental value has historically been relatively poorly known. In fact, several analyses[5,6,9] of falloff data from reaction 1, making use of an experimental determination[52] of the rate of reaction −1b, have suggested more importance for channel 1b than was observed experimentally. Product branching fractions were also found to be sensitive to the enthalpy of reaction 1b, and to fit observed experimental data, several authors have suggested an increase in the heat of

TABLE 1: Channel Energies and Stationary Point Energies at 0 K (kcal/mol)

stationary point	ATcT[a]	present[b]	ref 29[c]	ref 51[d]
$CH_3 + OH$	0.0	0.0	0.0	0.0
CH_3OH	-90.25 ± 0.05	−90.4	−91.9	−87.6
CH_3OH[e]		−89.8		−87.0
$^1CH_2 + H_2O$	0.58 ± 0.07	0.03	−1.6	0.5
$H_2 + H_2CO$	-69.92 ± 0.06	−70.0	−73.8	−68.2
H_2 + *cis*-HCOH	-13.13 ± 0.32	−13.8	−17.1	−12.3
H_2 + *trans*-HCOH	-17.77 ± 0.29	−18.0	−21.4	−16.4
$H + CH_2OH$	4.30 ± 0.09	4.6	4.3	7.5
$H + CH_3O$	13.75 ± 0.10	13.7	13.0	15.6
$^3CH_2 + H_2O$	-8.42 ± 0.06	−8.7	−11.2	
$CH_2 \cdots H_2O$ (vdW)		−8.5	−9.2	−4.8
$[^1CH_2 + H_2O \leftrightarrow CH_3OH]^‡$ (SP1)		−7.3	−7.8	−4.6
$[H_2 + H_2CO \leftrightarrow CH_3OH]^‡$ (SP2)		−0.3	−1.3	1.7
$[H_2$ + *cis*-HCOH $\leftrightarrow CH_3OH]^‡$ (SP3)		−2.2	−3.8	−0.6
$[H_2$ + *trans*-HCOH $\leftrightarrow CH_3OH]^‡$ (SP4)		−4.8	−6.4	−2.2
$[CH_3 + OH \leftrightarrow {}^3CH_2 + H_2O]^‡$ (SP5)		5.6	6.7	15.8

[a] Obtained from Active Thermochemical Tables ver. 1.35 and the Core (Argonne) Thermochemical Network v. 1.062. Uncertainties are given as 95% confidence limits (nearly equal to two standard deviations). [b] QCISD(T)/CBS//B3LYP/6-311++G**. [c] G2M(cc2)//B3LYP/6-311G(d,p). [d] MRCI+Q/CBS//CAS(10,10)/cc-pVDZ, where the CBS limit was extrapolated from the aug-cc-pVDZ and aug-cc-pVTZ basis sets. [e] Methanol in an eclipsed configuration.

formation of $^1CH_2$ by 2.6 (ref 5), 0.4 ± 0.5 (ref 6), and 2 (ref 9) kcal/mol relative to the value suggested in the 1987 Sandia database.[53] Recently,[54] the enthalpy of formation of $^1CH_2$ was revised upward by ∼1 kcal/mol, with the assigned experimental uncertainty reduced to 0.2 kcal/mol. In addition, the enthalpy of formation of one of the reactant species, OH, was recently revised downward by ∼0.5 kcal/mol.[40,55,56] The most recent IUPAC evaluation[57] adopts almost identical values for both species. The present ATcT analysis results in further refined values of 102.53 ± 0.06 kcal/mol (cf. to 102.5 ± 0.4 kcal/mol from the IUPAC recommendation[55]) for the enthalpy of formation for $^1CH_2$ at 298 K and 8.96 ± 0.02 for the enthalpy of formation of OH at 298 K (cf. to IUPAC's[55] 8.91 ± 0.07 kcal/mol). Compared to previous literature values, this further increases the energy of channel 1b relative to $CH_3 + OH$ and makes reaction 1b unambiguously endothermic with an enthalpy of 0.58 ± 0.07 kcal/mol at 0 K.

II.B. Theory. The energies of nonequilibrium species are not directly available from experiment and must be obtained from theory. Stationary point geometries, minimum energy paths, and vibrational frequencies were calculated using the B3LYP density functional[58] and the 6-311++G** basis set.[59] Barrier heights, fragment energies, and energies along minimum energy paths were computed by extrapolating QCISD(T)[60] energies to the complete basis set (CBS) limit using the formula[61]

$$E_{\mathrm{cc-pVxZ}} = E_{\mathrm{CBS}} + \frac{B}{(n_x + 1)^4} \qquad (3)$$

where $n_T = 3$ and $n_Q = 4$ for the cc-pVTZ and cc-pVQZ basis sets,[62] respectively.

The Q_1 diagnostic[63] was used to estimate the importance of multireference effects and thereby the reliability of the QCISD(T) calculations, where values larger than 0.02−0.04 are generally interpreted to indicate significant nondynamical correlation. For both the cc-pVTZ and cc-pVQZ basis sets, the Q_1 diagnostic was less than 0.02 for all the species listed in Table 1 except for SP5, which had a Q_1 diagnostic of 0.029, which is still reasonable.

The calculated energy of the OH fragment was lowered by 0.109 kcal/mol relative to the other fragments to account for the spin−orbit splitting of the $^2\Pi$ ground state into $^2\Pi_{3/2}$ and $^2\Pi_{1/2}$ states, as described by the Hill−Van Vleck[64] expression for the rotational terms in $^2\Pi$ (see, e.g., eq V,28 of ref 65).

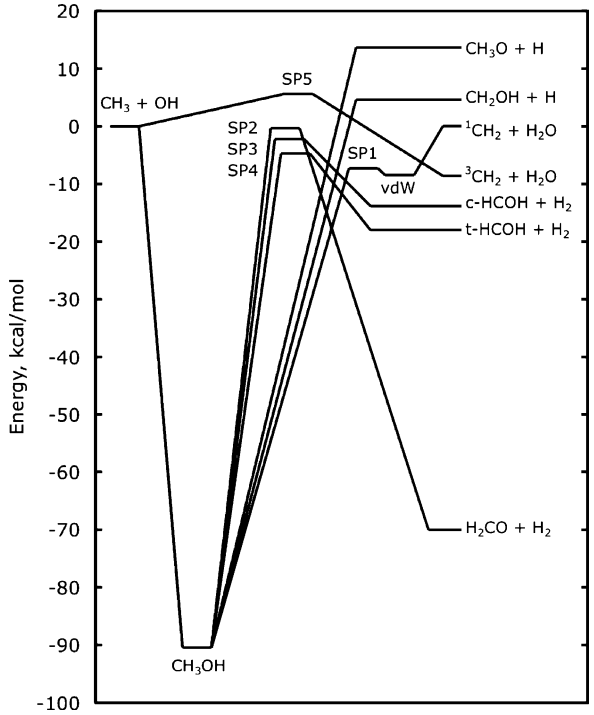

Figure 1. Zero-point inclusive stationary point energies computed at the QCISD(T)/CBS//B3LYP/6-311++G** level of theory.

This treatment includes angular momentum coupling of the rotational and electronic degrees of freedom.

The resulting zero-point inclusive QCISD(T)/CBS stationary point energies are shown schematically in Figure 1 and are summarized in Table 1, along with two recent sets of theoretical values[29,51] and the ATcT results discussed above. The present theoretical results agree well with the ATcT results, with an rms error of only 0.34 kcal/mol (corresponding to ∼0.7 kcal/mol when expressed as a 95% confidence limit, as is customary in experimental thermochemistry). The G2M(cc2)//B3LYP/6-311G(d,p) method[29] has an rms error of 2.6 kcal/mol, and the MRCI+Q/CBS//CAS(10,10)/cc-pVDZ method[51] has an rms error of 1.8 kcal/mol for this system.

A fairly significant discrepancy exists among the calculated values and the experimental value for the $^1CH_2 + H_2O$ channel energy. Due to the importance of this quantity in modeling the kinetics of reactions 1 and 2, we will briefly discuss the

calculated value. As shown in Table 1, previous theoretical studies have predicted the $CH_3 + OH \rightarrow {}^1CH_2 + H_2O$ reaction to be both exothermic,[29] endothermic,[51] and in the present calculation, nearly thermoneutral. We find the enthalpy for reaction 1b at 0 K, ΔH_r^{1b}, to be very sensitive to the size of the basis set or to the details of the basis set extrapolation. For example, using B3LYP/6-311++G** geometries and frequencies and the QCISD(T) method, the cc-pVDZ, cc-pVTZ, cc-pVQZ, cc-pV5Z, and cc-pV6Z basis sets predict 7.3, 3.0, 1.3, 0.58, and 0.38 kcal/mol for ΔH_r^{1b}, respectively. Optimizing the parameters B and E_{CBS} in eq 3 to best fit the series of results obtained for the five basis sets results in an extrapolated value for ΔH_r^{1b} of 0.30 kcal/mol, which is in reasonable agreement with the ATcT result. However, with the cc-pVDZ basis set excluded from the series during the extrapolation, a much better fit to eq 3 is obtained and the prediction falls to 0.03 kcal/mol. Using the CCSD(T) method, an extrapolation using all five basis sets predicts 0.14 kcal/mol for ΔH_r^{1b}, whereas excluding the cc-pVDZ basis set gives −0.11 kcal/mol. Similar trends and values were obtained for the series of augmented Dunning basis sets up to aug-cc-pV5Z for both the QCISD(T) and CCSD(T) methods. In ref 51, a multireference method (specifically, CASSCF with the cc-pVDZ basis set and an active space of ten electrons in ten orbitals) was used to optimize geometries, and an extrapolation was made to the complete basis set limit using the multireference configuration interaction method and the aug-cc-pVDZ and aug-cc-pVTZ basis sets. Their predicted value (0.5 kcal/mol) and the experimental result are in good agreement, which the authors tentatively attributed to the use of multireference geometries. We find that using B3LYP/6-311++G** geometries and extrapolating QCISD(T) energies from the aug-cc-pVDZ and aug-cc-pVTZ basis sets predicts an enthalpy of reaction of 0.92 kcal/mol, which is significantly higher than the more complete extrapolations discussed above. This analysis demonstrates the considerable uncertainty in extrapolating from just the aug-cc-pVDZ and aug-cc-pVTZ basis sets. Obtaining a more accurate theoretical value for ΔH_r^{1b} is beyond the scope of the present work.

A composite potential energy surface describing reactions 1 and 2 was obtained from the present theoretical and ATcT results as follows. Relative channel energies were taken directly from the ATcT results. Energies for the saddle points, the van der Waals well, and along the minimum energy paths were defined relative to their associated bimolecular fragments (CH_3 + OH, in the case of SP5) and were taken from the QCISD-(T)/CBS results reported in Table 1.

VRC-TST calculations were carried out by evaluating the potential energy directly. The QCISD(T) method with the aug-cc-pVDZ basis set[66] was used for the outer, barrierless region of the ${}^1CH_2 + H_2O$ channel. The CASPT2 method[67] with the cc-pVDZ, aug-cc-pVDZ, and aug-cc-pVTZ basis sets was used for the radical−radical association kinetics. In the CASPT2 calculations, the active orbitals and electrons were chosen to be the minimum required for qualitatively correct dissociation, i.e., three orbitals and four electrons for the CH_3 + OH and H + CH_3O reactions, and two orbitals and two electrons for the H + CH_2OH reaction. For the H + CH_3O reaction, optimized orbitals were obtained for the average energy of the two lowest-energy states.

Spin−orbit interactions split the four ${}^2\Pi$ states of OH into two doubly degenerate states, ${}^2\Pi_{3/2}$ and ${}^2\Pi_{1/2}$. For the CH_3 + OH reaction at large fragment separations, spin−orbit interactions split the degenerate set of two singlet and two triplet states into two pairs of singlet and triplet states that correlate with the ${}^2\Pi_{3/2}$ and ${}^2\Pi_{1/2}$ states of OH. At short fragment separations, however, the CH_3 + OH system may be characterized by a single uncoupled singlet electronic state. The change in the magnitude of the spin−orbit splitting along the reaction path for CH_3 + OH may have a kinetically measurable effect on the rate coefficient for the reaction, and spin−orbit splitting was included for the CH_3 + OH reaction as follows. Uncoupled energies for the two lowest-energy singlet states and the two lowest-energy triplet states were computed using state-averaged CASPT2 calculations and the cc-pVDZ, aug-cc-pVDZ, or aug-cc-pVTZ basis sets. Spin−orbit perturbations to the uncoupled energies were treated using state averaged CASSCF/6-311++G* wave functions and the Breit−Pauli operator,[68] and spin−orbit coupled energies were obtained by diagonalizing the resulting energy matrix. We also consider calculations where spin−orbit coupling was neglected in which the CASPT2 method was used with state averaged orbitals for the two lowest-energy singlet states. A level shift[69] of 0.2 hartree was used in the CASPT2 calculations for the CH_3 + OH reaction.

The Gaussian program package[70] was used to perform the density functional theory calculations and geometry optimizations, and the Molpro program package[71] was used to perform the QCISD(T), CASPT2, and spin−orbit calculations.

III. Kinetics

III.A. Transition State Theory. The direct VRC-TST method for computing rate coefficients for barrierless reactions was recently implemented in the computer code VaReCoF[72] and has been described in detail elsewhere.[43−45] Briefly, the VRC-TST method efficiently includes important couplings and anharmonicities in the nuclear motions by classifying them into two categories, as suggested by Wardlaw and Marcus.[73] Conserved nuclear modes correspond to vibrational motions of the separated fragments and are assumed to evolve adiabatically along the reaction path. Transitional nuclear modes correspond to rigid fragment rotations and translations at large separations and participate in bond formation, relative rotations, and overall rotation at intermediate distances. Transitional modes are often highly anharmonic, and an important feature of the VRC-TST method is that these modes are treated as fully anharmonic and coupled to one another. The conserved modes are assumed to be separable from the transitional ones, and the fragments are fixed at their asymptotic equilibrium geometries; i.e., fragment relaxation at finite fragment separations is neglected.

The effect on the overall rate coefficient of neglecting fragment relaxation is expected to be small for most barrierless reactions. For example, it was recently shown[47] for the CH_3 + CH_3 association reaction that the kinetic effect of the energy reduction in the evaluated potential energy along the minimum energy path due to relaxation was largely offset by an increase in the resulting vibrational frequencies. For Jahn−Teller distorted species such as CH_3O, however, an additional consideration arises. The CH_3O radical distorts away from C_{3v} symmetry to two C_{2v} species of A′ and A″ symmetry. At large fragment separations, the CH_3O + H interaction potentials for A′ and A″ geometries are similar in magnitude but correspond to different preferred approaches of the H atom to CH_3O. The preferred approach of the H atom to the A′ geometry is in the plane of symmetry of CH_3O, whereas the preferred approach to the A″ species is roughly perpendicular to the plane of symmetry. One might choose to compute rates for addition of the H atom to the A′ and A″ species separately and then average them to obtain an overall rate for CH_3O + H. However, at fragment separations of ∼2.5 Å, which is within the range of

transition state dividing surfaces considered in the present work, the interaction energy becomes comparable to the energy gap between the A′ and A″ electronic states (~3−4 kcal/mol), and the two pathways for addition become mixed. We chose to treat the $CH_3O + H$ reaction with CH_3O fixed at its optimal C_{3v} geometry, at which both pathways for addition are available. We note that the interaction potential for H atom with the C_{3v} geometry of CH_3O agrees well with the Jahn−Teller distorted interaction potentials, and we do not expect this approximation to be a significant source of error.

In the $CH_3O + H$ reaction, the reactant H atom may directly abstract an H atom to form $H_2 + CH_2O$. As we are interested in characterizing the transition state for $CH_3OH \rightarrow H + CH_3O$, we eliminated the direct abstraction channel from the overall rate by placing an infinite potential[45,74,75] along a plane perpendicular to the C−O bond and passing through the C atom of the CH_3O fragment.

The location of the optimal canonical transition state for barrierless reactions can vary significantly as a function of temperature. At low temperatures, one expects the rate to be controlled by centrifugal barriers located at relatively large fragment separations. When this is the case, transition state dividing surfaces defined in terms of fixed center of mass (CoM) separations are appropriate. At moderate and high temperatures, the centrifugal barriers move toward shorter fragment separations where chemical bonding begins to take place. For these temperatures, the variable reaction coordinate (VRC) approach is generally more accurate[43] (i.e., features less dynamical recrossing) than using CoM dividing surfaces. VRC dividing surfaces are obtained by defining a pivot point location for each fragment around which the fragments are allowed to rotate rigidly and then specifying a fixed distance between pivot points. The pivot points need not be located at an atomic center or at the center of mass of the fragment. For radical−radical reactions, pivot points are typically displaced from the atom participating in bond formation along the singly occupied orbital.

When multiple sites are available for bonding, multifaceted (MF) dividing surfaces, described in detail elsewhere,[75] are required. Briefly, multifaceted dividing surfaces are obtained by specifying the locations of two or more pivot points for one or both fragments and then specifying a minimum separation for each pair of pivot points located on different fragments. The overall dividing surface is obtained by considering geometries that do not violate any of the minimum separation criteria and that have at least one pivot point separation equal to its minimum allowed value. The resulting dividing surface is continuous and may therefore be variationally optimized.

In the present work, a combination of CoM, VRC, and MF dividing surfaces were used. CoM dividing surfaces were included for all of the VRC-TST calculations. For the $CH_3O + H$ reaction, VRC dividing surfaces were included with the pivot point for CH_3O displaced from the center of mass past the O atom along the C−O axis. MF dividing surfaces were included for the $CH_3 + OH$ reaction, with pivot points displaced along the 3-fold axis of CH_3, and for the $CH_2OH + H$ reaction, with pivot points located off the carbon atom and perpendicular to the plane defined by the two principal axes with the smallest moments of inertia (i.e., out of the "plane" of the nearly planar CH_2OH). For each choice of pivot point orientations, several pivot point displacements and fragment separation were considered, as summarized in Table 2.

Even for a fixed temperature, the optimal transition state dividing surface for a barrierless reaction may vary significantly as a function of total energy E and total angular momentum J.

TABLE 2: Pivot Point Specifications for the VRC-TST Calculations (bohr)[a]

system	type of dividing surface	interfragment distances
$CH_3 + OH$	CoM[b]	8(1)11, 13(2)19
	MF[c] $d = 0.5$	5(0.5)8
$^1CH_2 + H_2O$	CoM	6(0.5)9, 10(1)13, 15(2)19
$H + CH_2OH$	CoM	4(0.5)9, 10(1)13, 15(2)19
	MF $d = 0.5(0.5)2.0$	4(0.5)9
$H + CH_3O$	CoM	4(0.5)9, 10(1)13, 15(2)19
	VRC[d] $d = 0.5, 1.0$	4(0.5)7, 8(1)10

[a] 1 bohr = 0.5292 Å. $X(Y)Z$ denotes a grid of distances from X to Z in steps of Y. [b] Pivot points located at the centers of mass of both fragments. [c] Multifacted dividing surfaces with pairs of pivot points displaced from the C atom by the distance d. [d] Variable reaction coordinate dividing surfaces with a pivot point displaced from the O atom by the distance d.

We therefore performed our variational optimizations at the E,J-resolved level. The classical flux for the transitional modes $N_t(E,J)$ was evaluated for a given dividing surface by sampling over the transitional modes subject to the constraints of the dividing surface at fixed E and J. N_t was then variationally minimized for each E,J pair to obtain $N_t^{\ddagger}(E,J)$. The total flux $N^{\ddagger}(E,J)$ was obtained by convoluting the flux for the conserved modes obtained by directly counting states with the contribution from the transitional modes.

The harmonic oscillator approximation for the conserved modes is often surprisingly accurate, presumably because it neglects both the anharmonicity within each mode (which would tend to increase the partition function) and the couplings between modes (which would tend to decrease the partition function). However, the umbrella motion of CH_3 is especially poorly described by a harmonic potential,[76] and we therefore obtained energy levels for this mode numerically from the one-dimensional anharmonic potential for the umbrella motion reported in ref 76. For the remaining conserved modes, the harmonic oscillator approximation was used with frequencies fixed at their asymptotic values.

High-pressure limit thermal rate coefficients are related to the total flux at the transition state according to

$$k^{\infty}(T) = \kappa \frac{g_e \sigma}{h Q_v(T)\, Q_r(T)\, Q_t(T)} \sum_J \int \mathrm{d}E\, N^{\ddagger}(E,J) \mathrm{e}^{-E/k_B T} \quad (4)$$

where $N^{\ddagger}$ includes the rotational degeneracy $(2J + 1)$, κ is the transmission coefficient, g_e is the ratio of the electronic partition functions of the transition state species and the reactant fragments, σ is the ratio of the rotational symmetry numbers of the reactant fragments and the transition state species, Q_v and Q_r are the vibrational and rotational partition functions for the reactant fragments, Q_t is the relative translational partition function per unit volume, k_B is Boltzmann's constant, and T is temperature. As discussed above, the VRC-TST method neglects the coupling of the conserved modes to the transitional ones, and it can be shown[77] that under this and other related assumptions the contribution to the thermal rate from the conserved vibrational modes cancels out and

$$k^{\infty}(T) = \kappa \frac{g_e \sigma}{h Q_r(T)\, Q_t(T)} \sum_J \int \mathrm{d}E\, N_t^{\ddagger}(E,J) \mathrm{e}^{-E/k_B T} \quad (5)$$

One may choose to incorporate dynamical recrossing into eqs 4 and 5 by setting $\kappa < 1$. This factor has recently been estimated for hydrocarbon radical−radical association reactions involving hydrogen as a reacting partner[46] and for reactions involving two

hydrocarbon fragments,[47] where it was found to be 0.9 and 0.85, respectively. We do not pursue a detailed study of recrossing in the present work, and we set $\kappa = 0.9$ for the H + CH_2OH and H + CH_3O barrierless reactions and $\kappa = 0.85$ for the CH_3 + OH and $^1CH_2$ + H_2O barrierlesss reactions.

In the VRC-TST calculations, the electronic partition function for OH was treated as uncoupled to rotation, and as discussed in section II.B., an orientation dependent spin−orbit splitting was computed and included when evaluating N_t for the CH_3 + OH reaction. The neglect of rovibronic coupling (i.e., the angular momentum coupling of the electronic and rotational degrees of freedom) in OH can have a significant effect on the total partition function of OH, especially at low temperatures. We chose to treat the electronic partition function for OH classically and as uncoupled to rotation when computing rate coefficients from eqs 4 and 5. This choice may be justified in the high-pressure limit for association reactions involving OH if the contribution of the rovibronic coupling to the reactive flux at the transition state is similar to its asymptotic contribution. To test this, we computed the spin−orbit coupling for the CH_3 + OH reaction along the minimum energy path for association. The spin−orbit lowering of the ground state along the minimum energy path deviated from its asymptotic value (69 cm^{-1}) by less than ∼10% for C−O separations greater than 3 Å. This range includes the locations of the preferred canonical transition states for temperatures below 1000 K. At higher temperatures, the error caused by neglecting rovibronic coupling in the reactant OH fragment is expected to be small (the coupled and uncoupled electronic-rotational partition functions for OH differ by less than 5% at 1000 K and their agreement increases with temperature). Therefore, it is likely that the effects of rovibronic coupling on the partition function, when significant, are similar for the reactants and for the transition state species, and because we neglected rovibronic coupling when computing N_t, we computed the electronic partition function for the reactant OH as $2 + 2\exp(-137\ cm^{-1}/k_BT)$ and as uncoupled to rotation. The error introduced by neglecting rovibronic coupling in the pressure dependent association rates is less clear, although we expect this effect to be small for the reasons given above.

When rate coefficients are computed for dissociation, the integrated flux at the transition state is divided by the partition function for the dissociating complex. Therefore, for the rate describing methanol dissociation to CH_3 + OH, we would not observe the cancellation of the effects of rovibronic coupling in OH as discussed above for the bimolecular reaction at low temperature. In the present, work, however, we focus on high temperatures when considering dissociation, and we therefore neglected rovibronic coupling in the rate calculations for dissociation as well.

Reactions with saddle points were treated using variational TST and the rigid rotor and harmonic oscillator approximations with several corrections. The potential energy for the saddle point and along the minimum energy path was evaluated using the QCISD(T)/CBS method and B3LYP/6-311++G** geometries, as discussed above. Tunneling was included using the asymmetric Eckart formula.[78] Torsional motions were identified and treated as hindered rotors. Projected vibrational frequencies were evaluated along the minimum energy path at the B3LYP/6-311++G** level of theory using both Cartesian and curvilinear coordinates.[79−81] Differences in the computed rate coefficients using these two sets of frequencies are discussed in section IV for the CH_3 + OH → $^3CH_2$ + H_2O reaction. For the remaining transition state regions with saddle points, the choice of coordinate systems for obtaining projected frequencies is expected to have a negligible effect on the overall rate coefficients for reactions 1 and 2, and Cartesian coordinates were used. Projected frequencies using curvilinear coordinates were calculated with the POLYRATE program package[82] and the algorithm described in ref 81.

As shown in Figure 1 and as discussed in the Introduction, the $^1CH_2$ + H_2O channel has a saddle point barrier (SP1) and a van der Waals (vdW) minimum 7.3 and 8.5 kcal/mol lower than those of the separated fragments, respectively. At low temperatures, one expects the overall rate to be controlled by an outer transition state region corresponding to centrifugal barriers at large fragment separations. At high temperatures, one expects an inner transition state associated with the saddle point SP1 to be the dynamical bottleneck. At intermediate temperatures, both transition state regions may contribute to the overall rate, and the error resulting from neglecting one of the transition state regions can be significant.

We computed $N^{\ddagger}_{1b}$ using a unified statistical model,[49,83,84]

$$\frac{1}{N^{\ddagger}_{1b}(E,J)} = \frac{1}{N^{\ddagger}_{inner}} + \frac{1}{N^{\ddagger}_{outer}} - \frac{1}{N_{max}} \tag{6}$$

where $N^{\ddagger}_{inner}$ is the variationally optimized flux at SP1 computed using the harmonic oscillator and rigid rotor approximations with an asymmetric Eckart tunneling correction, $N^{\ddagger}_{outer}$ is the flux for the barrierless association computed using ab initio VRC-TST at the QCISD(T)/aug-cc-pVDZ level, and N_{max} is the (approximate) maximum flux between the inner and outer transition state regions. To obtain N_{max}, we considered the set of outer (VRC-TST) dividing surfaces as well as several along the minimum energy path connecting SP1 with vdW for the inner transition state. We approximated N_{max} as the maximum of N_{vdW} and N_{outer} for center of mass separations equal to 3.2 Å. We found that simply neglecting $1/N_{max}$ (i.e., assuming N_{max} is large) did not significantly alter the overall rate coefficient, and we therefore do not pursue a more detailed evaluation of N_{max}.

The *E,J*-resolved variational TST calculations were carried out using Variflex.[85]

III.B. Master Equation Simulations. Pressure dependent rate coefficients were obtained via master equation simulations, as described elsewhere.[86,87] For methanol dissociation, the two-dimensional (*E,J*) master equation was solved by writing the collisional energy transfer function as[87]

$$P(E,J;E',J') = P(E,E')\,\phi(E,J) \tag{7}$$

where primed and unprimed quantities denote the state of the system before and after the collision, respectively. The factorization in eq 7 assumes that collisional energy transfer is independent of J' and that J and J' are not correlated. The function $\phi(E,J)$ is the fractional contribution to the total density of states at energy E from angular momentum J and was specified as in the "*E,J* model" of ref 87. $P(E,E')$ was modeled by a single exponential down function and an average downward energy transfer given by

$$\langle \Delta E_d \rangle = \alpha \left(\frac{T}{300\ K} \right)^{\gamma} \tag{8}$$

with $\alpha = 133\ cm^{-1}$ and $\gamma = 0.8$. This form for $\langle \Delta E_d \rangle$ is quite reasonable, and similar forms have previously been used to model reactions on the C_3H_4 potential energy surface[88] as well as reactions of OH with acetylene[89] and ethylene.[48] We also considered the one-dimensional (*E*) master equation for dis-

TABLE 3: High-Pressure Limit Rate Coefficients Fit to $A(T/300\ \mathrm{K})^n \exp(-E/T)$ for $T = 300-2500$ K

reaction	A (cm^3 molecule^{-1} s^{-1})	n	E (K)
$CH_3 + OH$[a]	9.305×10^{-11}	−0.01761	−16.74
$CH_3 + OH \rightarrow {}^3CH_2 + H_2O$[b]	1.638×10^{-13}	2.568	2012
$^1CH_2 + H_2O$[c]	2.053×10^{-12}	0.8750	718.7
	2.558×10^{-10}	−2.182	163.6
$H_2 + H_2CO$	2.285×10^{-11}	0.0	35080
$H_2 +$ *trans*-HCOH	1.270×10^{-14}	2.621	4477
$H_2 +$ *cis*-HCOH	3.153×10^{-14}	2.270	4125
$H + CH_3O$	1.594×10^{-10}	0.2397	−26.11
$H + CH_2OH$	2.887×10^{-10}	0.04166	0.0

[a] VRC-TST with CASPT2/aug-cc-pVTZ. [b] Direct abstraction on the triplet surface. [c] Rate coefficients for this reaction were fit to the sum of two modified Arrhenius expressions, and both sets of parameters are given.

sociation, where the rotational distribution is assumed to remain thermally distributed throughout the reaction, and we found that the one-dimensional and two-dimensional treatments agree well for methanol dissociation. The two-dimensional treatment is not readily applicable to bimolecular reactions, and the one-dimensional master equation was used exclusively when modeling pressure dependence in reaction 1.

For the bimolecular reaction calculations, the "initial-rate" and "long-time" methods[87] for obtaining phenomenological rates from the master equation gave similar results for the total rate for most conditions. When the results differed, they typically did so by less than 2%. For dissociation, the "initial rate" method was used exclusively. An energy step size of 50 cm^{-1} was used with an energy range $E = -32\,000$ to $+40\,000$ cm^{-1}, except for dissociation at low temperatures where $E = -12\,500$ to $+30\,000$ cm^{-1}. The total angular momentum grid consisted of a step size of 6 $\hbar$ and a range of $J = 0-300\ \hbar$. Collision cross sections were obtained using[90] $\sigma_{He} = 2.57$ Å, $\sigma_{Ar} = 3.41$ Å, $\sigma_{Kr} = 3.60$ Å, $\sigma_{CH_3OH} = 3.63$ Å, $\epsilon_{He} = 7.1$ cm^{-1}, $\epsilon_{Ar} = 85$ cm^{-1}, $\epsilon_{Kr} = 120$ cm^{-1}, and $\epsilon_{CH_3OH} = 335$ cm^{-1}. Geometries, vibrational frequencies, and rotational constants are provided as Supporting Information.

Master equation simulations were performed using Variflex.[85]

IV. Results and Discussion

IV.A. Capture Rates for the Bimolecular Channels. In this section, capture rate coefficients are presented for the $CH_3 + OH$ reaction and for the reverse reactions associated with the bimolecular product channels of reactions 1 and 2, and the results are compared with previous theoretical and experimental results. The best present theoretical prediction for the capture rate coefficient for each reaction was fit to a modified Arrhenius expression,

$$k(T) = A(T/300\ \mathrm{K})^n \exp(-E/T) \qquad (9)$$

and the results are summarized in Table 3.

$CH_3 + OH$. Rate coefficients for the $CH_3 + OH$ association reaction in the high-pressure limit were calculated using VRC-TST, as discussed in section III. Fragment interaction energies were evaluated directly at the CASPT2 level of theory for three basis sets, cc-pVDZ, aug-cc-pVDZ, and aug-cc-pVTZ, and the resulting rate coefficients are shown in Figure 2.

For this reaction, the CASPT2/cc-pVDZ potential energy surface contains unphysical wells at hydrogen-bonding configurations resulting from basis set superposition effects. The addition of diffuse basis functions (as in the augmented Dunning basis sets) was found to remove these spurious wells. The cc-pVDZ interaction energy along the minimum energy path for association is less attractive than for the augmented basis sets, but due to the artificial wells in the cc-pVDZ surface, the rate

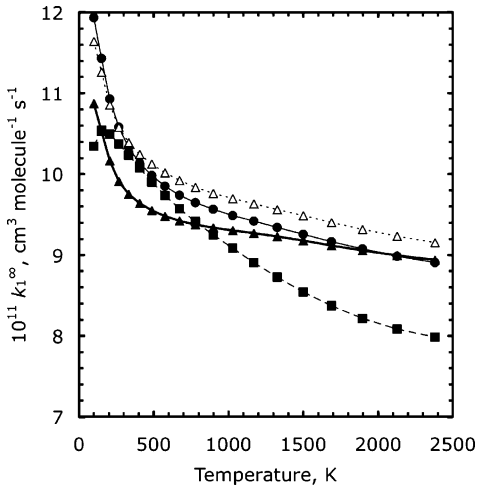

Figure 2. Dynamically corrected VRC-TST rate coefficients for the $CH_3 + OH$ reaction computed using the CASPT2 method and including spin−orbit splitting for the cc-pVDZ (filled squares), aug-cc-pVDZ (filled circles), and aug-cc-pVTZ (filled triangles) basis sets and for the CASPT2/aug-cc-pVTZ surface with spin−orbit splitting neglected (open triangles).

coefficients computed for all three basis sets are similar in magnitude for temperatures less than ~1000 K. The temperature dependence of the rate coefficient predicted with the cc-pVDZ basis set, however, is qualitatively incorrect.

We note that the CASPT2/cc-pVDZ potential energy surface was found to be qualitatively correct for hydrocarbon fragments,[46,47] where it was shown that one-dimensional correction potentials could be used to correct the CASPT2/cc-pVDZ energies to obtain quantitatively accurate rate coefficients. The correction potential strategy is not suitable for $CH_3 + OH$ due to the deficiencies of the CASPT2/cc-pVDZ potential energy surface discussed above and results in rate coefficients which are approximately 15% too high.

At room temperature, the rate coefficients computed using the two augmented basis sets differ by only 6%, and their agreement improves at higher temperatures. These results suggest that the VRC-TST calculations are well converged with respect to the basis set at the aug-cc-pVTZ level, and larger basis sets were not considered.

Also shown in Figure 2 is the rate coefficient computed for the CASPT2/aug-cc-pVTZ interaction potential with spin−orbit coupling neglected. The effect of including spin−orbit coupling when evaluating the flux for the transitional modes at the transition state is small and reduces the rate coefficient by only 2−7%.

Figure 3 shows the dynamically corrected VRC-TST rate coefficient, including spin−orbit coupling, for the aug-cc-pVTZ basis set along with several experimental determinations[3−7,9,10]

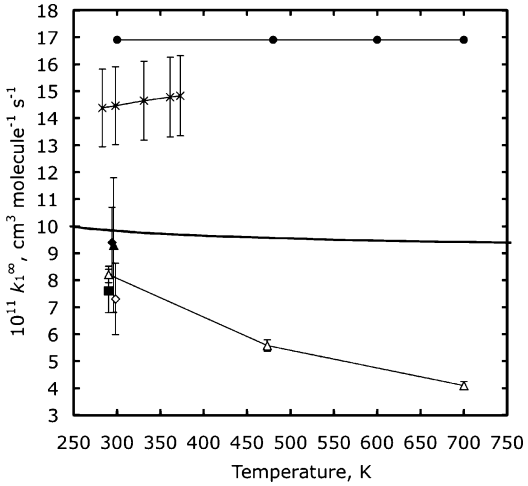

Figure 3. High-pressure limit rate coefficient for the $CH_3 + OH$ reaction. The present theoretical result is shown as a thick solid line. Also shown are several experimental results: Sworski et al.[3] (filled triangle), Anastasi et al.[4] (filled diamond), Hughes et al.[5] (filled square), De Avillez Pereira et al.[6] (open triangles), Deters et al.[7] (open diamond), Oser et al.[9] (filled circles), and Fagerström et al.[10] (x).

near room temperature and up to 700 K. At room temperature, the computed rate coefficient (9.82×10^{-11} cm^3 molecule^{-1} s^{-1}) is significantly lower than the results of Grotheer and co-workers[9] and Fagerström et al.[10] Grotheer and co-workers extrapolated from low pressures (less than 10 Torr) and under conditions where channel 1b was suppressed, and they therefore assigned considerable uncertainty to their reported value. As pointed out elsewhere,[7] the experimental conditions in ref 10 are such that the simulations used to obtain the high-pressure limiting rate coefficient may be relatively insensitive to the fitted value of k_1^∞. The present result agrees well with the results of Sworski et al.[3] and Anastasi et al.[4] and is only ~20−35% higher than three other room-temperature determinations,[5−7] including the recommended value of Baulch et al.[8] based on ref 6.

Next we consider the temperature dependence of k_1^∞. The VRC-TST result shows very little temperature dependence over the entire temperature range considered (300−2500 K). Grotheer and co-workers[9] and Fagerström et al.[10] reported little or no temperature dependence up to 373 and 700 K, respectively. De Avillez Pereira et al.,[6] in contrast, reported high-pressure limit rate coefficients that decreased by a factor of 2 as the temperature increased from 298 to 700 K, and this determination was recommended in a recent literature review.[8] In their study, the high-pressure limiting rate coefficients were obtained by extrapolating from experimental results at 8−700 Torr, and the authors reported that significant pressure dependence was not observed over this pressure range. We will discuss the pressure dependence of the $CH_3 + OH$ reaction in detail in section IV.B. We note here that the present calculations predict significantly more falloff below 1 atm at elevated temperatures than was reported in ref 6, such that our finite pressure rates agree well with the finite pressure measurements made in that study but our high-pressure limits differ significantly.

A comparison of several previous theoretical predictions for k_1^∞ is shown in Figure 4. At 298 K, these predictions vary by more than an order of magnitude from 1.5×10^{-11} cm^3 molecule^{-1} s^{-1} (ref 30) to $1.7-2.2 \times 10^{-10}$ (refs 29 and 31). Ing et al.[30] performed a QRRK calculation using a composite ab initio method (CBS-APNO) for the reverse rate (−1a) and then used microscopic reversibility to obtain k_1^∞. An empirical

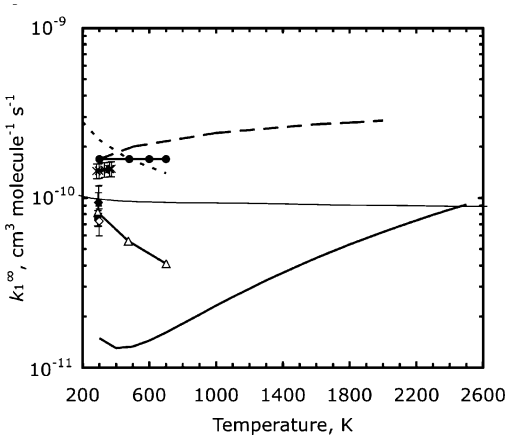

Figure 4. Comparison of the several theoretical predictions for the high-pressure limit rate coefficient for the $CH_3 + OH$ reaction: this work (thin line), Xia et al.[29] (dotted line), Jordan et al.[31] (dashed line), and Ing et al.[30] (thick solid line). Symbols indicate experimental results, as in Figure 3.

model for the fragment interaction energy was used in ref 31, and the reported results are therefore not expected to be quantitative.

The computed rate coefficient of Xia et al.[29] differs from the present calculated value by almost a factor of 2 at 298 K. Furthermore, the prediction of Xia et al. decreases by a factor of 2 from 200 to 700 K, whereas the rate coefficient reported here is nearly constant with respect to temperature. Xia et al. used the G2M method to parametrize a model for the interaction energy of $CH_3 + OH$, and generally, one might expect similar accuracies for the G2M method and the method used in the present work (CASPT2). However, radical−radical association reactions are poorly described by single-reference methods, especially at extended fragment separations, where multireference methods, such as CASPT2, are needed. There are also important differences in the two treatments of the barrierless transition state. First, the present treatment does not neglect the couplings and anharmonicities present in the $CH_3 + OH$ interfragment potential energy surface. Second, Xia et al. considered transition state dividing surfaces with fragment separations varying from 2.1 to 3.5 Å, whereas our set of dividing surfaces extends to fragment separations of 10 Å. We find that if we consider a set of CoM dividing surfaces with fragment separations less than 3.7 Å, we predict a rate coefficient that varies with temperature and that is greater than the result of our more accurate calculation by 100% at room temperature and by 15% at 1000 K. As discussed above, dividing surfaces located at large fragment separations are important for accurately computing rate coefficients for low temperatures.

$^1CH_2 + H_2O$. This channel features two distinct dynamical regimes and was modeled using eq 6, as discussed above. The resulting capture rate coefficient for the $^1CH_2 + H_2O$ reaction is denoted k_{-1b}^∞. For comparison, we also present rate coefficients for each of the transition state regions treated separately (k_{inner}^∞ and k_{outer}^∞), as well as the canonically coupled overall rate coefficient given by

$$k_{-1b}^{C,\infty}(T) = \frac{k_{inner}^\infty k_{outer}^\infty}{k_{inner}^\infty + k_{outer}^\infty} \qquad (10)$$

The rate coefficients are shown in Figure 5.

The flux for the inner transition state was variationally optimized for each *E*,*J* pair over a set of 10 dividing surfaces

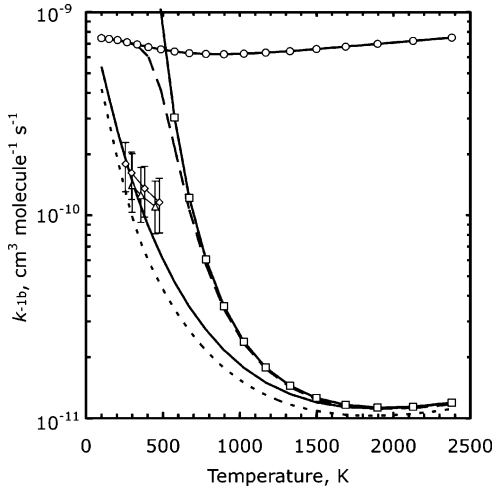

Figure 5. High-pressure limit rate coefficient for the $^1CH_2 + H_2O$ reaction for the inner transition state only (squares), the outer transition state only (circles), the canonically coupled result of eq 10 (dashed line), and the microcanonically coupled result of eq 6 (solid line). Also shown are two sets of experimental results obtained at 0.1−10 Torr: refs 91 and 93 (triangles) and refs 52 and 92 (diamonds), as well as the predicted microcanonically coupled rate coefficient at 1 Torr (dotted line).

along the B3LYP/6-311++G** minimum energy path extending ∼0.9 amu$^{1/2}$ bohr from the transition state. The geometry at the inner saddle point (SP1) contains a torsional motion with a frequency of 452 cm^{-1}. The van der Waals (vdW) well, which has a geometry similar to that for SP1, has a torsional frequency of 76 cm^{-1} and torsional barrier height of ∼5 kcal/mol. We assume that the larger frequency for the torsion at SP1 indicates a torsional barrier significantly larger than 5 kcal/mol, and we treat the torsion at SP1 as a harmonic oscillator. Variational effects were found to reduce both k^{∞}_{inner} and k^{∞}_{-1b} by ∼8% at 2000 K and by less than 1% at room temperature. The asymmetric Eckart tunneling correction increased k^{∞}_{inner} by ∼30% at room temperature and less than 2% at temperatures above 1000 K but had a negligible effect on k^{∞}_{-1b} for the entire temperature range considered.

Next we consider the outer, barrierless transition state. For this reaction, the set of dividing surfaces was defined in terms of fixed CoM separations, as shown in Table 2. For systems with an isolated barrierless transition state, if a suitable range of center of mass distances is used, a minimum in the classical flux is observed for each *E*,*J* pair when the flux is plotted as a function of fragment separation, and this minimum corresponds to the variationally optimized flux. In the present calculation, however, the presence of the inner saddle point near the barrierless region places a restriction on the range of center of mass distances included in the "outer" transition state region such that a minimum in the flux cannot always be observed. At SP1 the C−O separation is 1.9 Å, and, at 2.3 Å, the energy along the minimum energy path for the process $^1CH_2 + H_2O \rightarrow$ vdW equals the energy of SP1. It is therefore reasonable to restrict the set of dividing surfaces to those with CoM distances larger than ∼2.3 Å. The optimal distance at which to cut off the VRC-TST calculation, however, is not entirely clear. The results presented in Figure 5 were obtained using dividing surfaces with CoM fragment separations greater than or equal to 3.2 Å. We tested the effect of extending the range of CoM dividing surfaces to 2.6 Å, and this change reduced k^{∞}_{outer} by 23% and 68% at 300 and 2000 K, respectively. However, the effect on k^{∞}_{-1b} was negligible at room temperature and was only 3% at 2000 K. We conclude that, for this reaction, the separation of the overall rate coefficient into thermally averaged contributions from an outer barrierless transition state region and an inner saddle point is not appropriate. The computed value of k^{∞}_{outer} therefore depends sensitively on the details of this arbitrary separation, whereas the overall rate coefficient k^{∞}_{-1b} does not.

Rate coefficients for the depletion of $^1CH_2$ in the presence of water have been measured at room temperature[52,91] and at temperatures up to 475 K.[92,93] A direct comparison of the computed rate coefficients presented here to experimental ones is complicated by several factors. The experimentally determined rate coefficients include contributions from collision induced intersystem crossing $^1CH_2 \rightarrow {}^3CH_2$ in addition to the reaction of methylene with water, and the former process is estimated[52,92] to contribute anywhere from 0−50% to the total depletion rate. Rapid nonreactive quenching of $^1CH_2$ has been observed for a variety of atomic and molecular colliders and has been proposed[94] to occur via collision-induced perturbations of "gateway" rovibrational states of methylene. For reactive molecular colliders, such as water, an additional decay pathway is possible in which the reactive singlet surface crosses a nonreactive triplet surface, and the system proceeds nonreactively via a curve crossing to form $^3CH_2$. A determination of the relative importance of the two decay mechanisms is beyond the scope of the present work, and for comparison to the predicted rate coefficients shown in Figure 5, we simply reduce the experimental values by 25% (as suggested elsewhere[52]) to approximately remove contributions in the measured values arising from nonreactive quenching. The error bars shown in Figure 5 include an additional 25% uncertainty due to the unknown rate for intersystem crossing.

We note that in the master equation simulations discussed in sections IV.B and IV.C the fluxes calculated in this section are used to characterize the process $CH_3OH^* \rightarrow {}^1CH_2 + H_2O$, in which, to a first approximation, the system proceeds via SP1 to form a transient species associated with the van der Waals complex. This complex may then decay via the outer transition state to form $^1CH_2 + H_2O$. Intersystem crossing provides an additional decay pathway for the van der Waals complex, one which leads to the formation of $^3CH_2 + H_2O$. The theoretical treatment discussed above corresponds to the limit where the rate for intersystem crossing is small and may be neglected.

We may estimate a reasonable upper limit on the effect of including intersystem crossing in the master equation simulations by assuming that the rate for intersystem crossing is much faster than the rate for decay through the outer transition state region. Xia et al.[29] determined the minimum energy geometry along the seam of singlet−triplet crossings (MSX) at the G2M level of theory to occur at a C−O separation of 2.5 Å, which is intermediate of the van der Waals complex and the dividing surfaces used to describe the outer transition state region discussed above. The MSX was calculated[29] to have an energy 4.3 kcal/mol higher than the energy of the van der Waals complex, 2.9 kcal/mol higher than the energy of the inner saddle point (SP1), and 2.7 kcal/mol lower than the energy of the $^1CH_2 + H_2O$ products. In the limit of fast intersystem crossing, systems reaching MSX decay immediately to $^3CH_2 + H_2O$ and flux through the outer transition state region associated with molecular configurations to the product side of MSX (i.e., with C−O separations greater than ∼2.5 Å) no longer determines the rate for loss of CH_3OH^*. We model this limit using eq 6, with $N^{\ddagger}_{outer}$ replaced by the variationally optimized flux computed using the VRC-TST method for two dividing surfaces with fixed center of mass separations of 2.1 and 2.4 Å, and

with $1/N_{max}$ neglected. The effect of this modification on the results of the master equation simulations for reactions 1 and 2 is discussed briefly in sections IV.B and IV.C.

The experimental measurements were carried out at low pressures (0.1−10 Torr), whereas k_{-1b}^{∞} shown in Figure 5 represents the high-pressure limit. Master equation simulations were performed to assess the pressure dependence of the $^1CH_2 + H_2O$ reaction. At 300, 1000, and 2000 K, the predicted rate coefficient at 1 Torr is 33%, 16%, and 7% lower than the respective high-pressure limits, as shown in Figure 5. Stabilization is the most important decay pathway at room temperature and pressures above ∼10 Torr, whereas, at elevated temperatures, $CH_3 + OH$ is the most important product channel up to at least 10^5 Torr, the highest pressure considered here.

At room temperature, the adjusted experimental values of $(1.6 \pm 0.4) \times 10^{-10}$ (refs 52 and 92) and $(1.4 \pm 0.4) \times 10^{-10}$ cm^3 molecule^{-1} s^{-1} (refs 91 and 92) are in fair agreement with the computed value of 9.8×10^{-11} cm^3 molecule^{-1} s^{-1} at 1 Torr and 1.5×10^{-10} cm^3 molecule^{-1} s^{-1} for the high-pressure limit. The experimentally observed temperature dependence is not as strong as in the computed rate coefficients, and uncertainties in the temperature dependence of the rate of collision induced intersystem crossing could explain this difference. A positive temperature dependence for intersystem crossing in CH_2 for some molecular colliders has been reported.[94]

It is interesting to note that neither k_{inner}^{∞} nor k_{outer}^{∞} is a good approximation to k_{-1b}^{∞} for temperatures less than ∼1000 K. At low temperatures k_{-1b}^{∞} is expected to tend toward k_{outer}^{∞}. However, at 100 K, the lowest temperature considered, the two rates are only slowly convergent. Coupling the two transition state regions canonically, i.e., according to eq 10, overestimates the rate by almost a factor of 5 at room temperature when compared with the microcanonically coupled rate computed using eq 6.

In previous theoretical treatments of the kinetics of $^1CH_2 + H_2O$, the two transition state regions were considered separately[29] or either the inner[6] or the outer[30] transition state region was neglected. In some previous analyses[18,42] of reactions 1 and 2, k_{-1b}^{∞} was set equal to the room-temperature experimental value and was assumed to be independent of temperature. This assumption overestimates our predicted rate coefficient by more than a factor of 10 at temperatures above 1500 K.

Due to the importance of this channel, we tested the sensitivity of the computed rate coefficient on the saddle point energy. The energy of SP1 was lowered by 1 kcal/mol relative to the energy of $^1CH_2 + H_2O$, and this adjustment increases the rate coefficient by 25−50% over the temperature range shown.

H_2 + cis-HCOH, trans-HCOH, and H_2CO. As shown in Figure 1, the H_2 product channels have significant forward barrier heights relative to CH_3OH and are exothermic relative to $CH_3 + OH$. At low temperatures, where Boltzmann factors for energized species of CH_3OH are small and tunneling is the dominant decay mechanism, one may expect these channels to become important for reactions 1 and 2. Rate coefficients were computed as discussed in section III. The transition state was treated variationally for the *cis*-HCOH and *trans*-HCOH channels, and an Eckart tunneling correction was included for all three H_2 channels.

The predicted rate coefficient for the H_2 + *cis*-HCOH reaction is 2 and 1.5 times faster than the rate coefficient for the H_2 + *trans*-HCOH reaction at 1000 and 2000 K, respectively. The rate coefficient for the $H_2 + H_2CO$ reaction is several orders of magnitude smaller for the same temperature range.

$H + CH_3O$ and CH_2OH. As shown in Figure 1, the energized CH_3OH^* complex can dissociate barrierlessly to form $H + CH_3O$ and $H + CH_2OH$ and both processes are significantly endothermic. Rate coefficients were obtained for the $H + CH_3O$ and $H + CH_2OH$ association reactions using the VRC-TST method, as discussed in section III.

The calculated rate coefficient for $H + CH_3O$ ($(1.7-2.7) \times 10^{-10}$ cm^3 molecule^{-1} s^{-1} for 300−2500 K) is 4−6 times greater than the experimental results of Dobe et al.[95] at 300−500 K and 1−3 Torr. The magnitude of this discrepancy is significantly larger than typical errors reported for rate coefficients predicted using the VRC-TST method for radical−radical reactions involving H atom as a reacting partner,[46] which suggests the need for reinvestigating this reaction experimentally. In a previous[6] master equation simulation of reaction 1, the reverse rate for reaction 1g was assumed to be independent of temperature, and the value used (1.3×10^{-11} cm^3 molecule^{-1} s^{-1}) is 15−20 times lower than the present predicted value.

Rate coefficients for the association reaction $H + CH_2OH$ were obtained using the CASPT2 method and aug-cc-pVDZ basis set and separately using the correction potential (CP) scheme presented in ref 46. The CP is designed to correct CASPT2/cc-pVDZ energies to approximate Davidson-corrected multireference CI with singles and doubles (CAS+1+2) energies obtained with the aug-cc-pVTZ basis set. The rate coefficients computed using the CASPT2/aug-cc-pVDZ and the CP methods (∼3×10^{-10} cm^3 molecule^{-1} s^{-1}) agree well with each other. Due to the success of the CP scheme for radical−radical association reactions, we use the values based on the CP scheme in the master equations calculations in sections IV.B and IV.C. In the master equation simulations presented in ref 6, the reverse rate for channels 1g was assumed to be independent of temperature, and the value used (1.6×10^{-10} cm^3 molecule^{-1} s^{-1}) is approximately half the present predicted value.

$CH_3 + OH \rightarrow {}^3CH_2 + H_2O$. The abstraction of a hydrogen atom from CH_3 by OH may proceed on the triplet surface without forming a CH_3OH^* intermediate. This process has been predicted[96] to compete with the stabilization/dissociation pathway at high temperatures. In two previous theoretical studies of this reaction, Wilson and Balint-Kurti[96] and Xia et al.[29] presented forward barrier heights for the direct abstraction (1h) at several levels of theory, and their best estimates of the zero-point inclusive forward barrier height were 6.0 kcal/mol (QCISD(T)/cc-pVQZ//MP2/cc-pVDZ) and 6.7 kcal/mol (G2M(cc2)//B3LYP/6-311G(d,p)), respectively. The lower value agrees well with our predicted value of 5.6 kcal/mol computed at the QCISD(T)/CBS//B3LYP/6-311++G** level of theory.

In the present study, rate coefficients for this reaction were found to be sensitive to the treatment of the variational transition state. We consider canonical rate coefficients for three sets of dividing surfaces labeled SP5 (the B3LYP/6-311++G** optimized transition state), SP5′ (the location of the maximum zero-point inclusive QCISD(T)/CBS energy along the B3LYP/6-311++G** minimum energy path), and VTST (a set of 15 dividing surfaces along the B3LYP/6-311++G** minimum energy path). The barrier at SP5′ is 1.4 kcal/mol higher and displaced along the minimum energy path by ∼0.4 bohr amu$^{1/2}$ relative to the B3LYP/6-311++G** barrier. This results in a zero-point inclusive barrier of 7.1 kcal/mol at SP5′, which agrees well with the prediction of Xia et al.[29] The canonical rate coefficient for SP5′ is lowered by ∼85% at room temperature and ∼8% at 2000 K relative to the canonical rate coefficient for SP5. Optimizing the dividing surface as a function of temperature (as in the VTST calculation) further reduces the canonical rate coefficients by 1% at room temperature and by 12% at 2000 K relative to the SP5′ result. Similar trends were

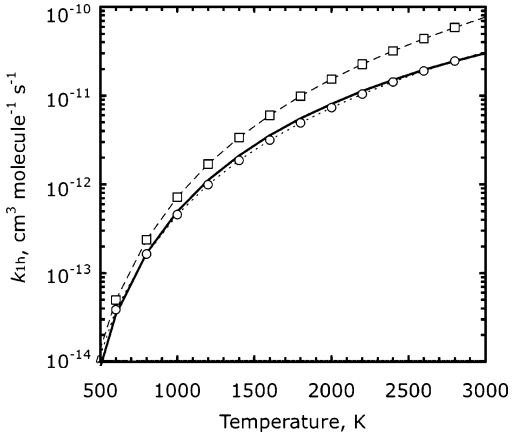

Figure 6. Rate coefficient for the $CH_3 + OH \rightarrow {}^3CH_2 + H_2O$ abstraction on the triplet surface (solid line). Also shown are the previous theoretical predictions of Wilson and Balint-Kurti[96] (circles) and Xia et al.[29] (squares).

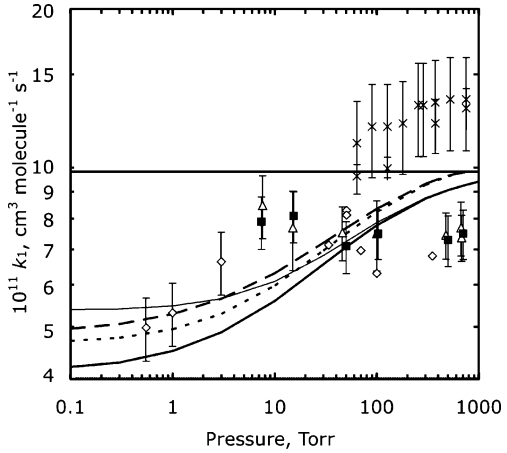

Figure 7. Falloff curve for the $CH_3 + OH$ bimolecular reaction at 298 K in He (thick solid line). The high-pressure limit is shown as a horizontal line. Several experimental results are shown using the same symbols as in Figure 3. The effects of lowering SP1 by 1 kcal/mol (dotted line), lowering all three H_2 channel barrier heights by 1 kcal/mol (dashed line), and using the theoretical value for the energy of channel 1b (thin line) are also shown.

observed when *E*,*J*-resolved rate coefficients were compared for the above sets of dividing surfaces.

The lowest harmonic frequency at the QCISD(T)/CBS transition state is 100 cm^{-1} and corresponds to the torsional motion of the OH and CH_2 fragments around the nearly linear $C-H_t-O$ atoms, where H_t is the hydrogen atom being transferred and the C−O distance is 2.5 Å. Because of the looseness of the transition state, it was difficult to calculate the barrier to rotation without artificially constraining the geometry. For planar geometries, a B3LYP/6-311++G** second-order saddle point was found 0.3 kcal/mol above SP5′, and due to the symmetry at the saddle point this represents an upper bound on the torsional barrier. If the planar second-order saddle point is allowed to relax to nonplanar geometries, a second-order saddle point could not be found. Treating this degree of freedom as a free rotor has a significant effect on the rate coefficient, reducing it by 9% at room temperature and 60% at 2000 K. Treating the torsion as a hindered rotor represented by a single sine function with a period of 180° results in rate coefficients similar to those obtained using the free rotor approximation for torsional barrier heights up to 0.7 kcal/mol, which is likely much larger than the true torsional barrier. In the results reported below, a hindered rotor with a barrier height of 0.3 kcal/mol was used.

We note that two other low-frequency (<400 cm^{-1}) degrees of freedom are strongly coupled to one another and to the torsional mode, suggesting that these degrees of freedom may not be well represented by the HO approximation. We do not pursue a more rigorous calculation of these modes in the present work.

Treating the umbrella motion in the CH_3 fragment as anharmonic, as discussed in section III, has a significant effect on the computed rate coefficient, increasing it by 20−35% for 1000−2500 K relative to treating the CH_3 umbrella motion as a harmonic oscillator. Rate coefficients computed using curvilinear coordinates to obtain the projected frequencies along the reaction path are ∼20% lower than those computed using Cartesian coordinates.

Wilson and Balint-Kurti[96] found that the inclusion of multidimensional (specifically, small curvature[97]) tunneling increased their rate coefficient by 160% at room temperature and had a negligible effect at 2000 K. We find that including an asymmetric Eckhart tunneling correction increases our computed rate coefficient by ∼250% at room temperature and by only 2% at 2000 K. At low temperatures, where the differences between the two treatments of tunneling are most significant, this process is not expected to contribute significantly to reaction 1, and a multidimensional tunneling correction was not pursued here.

Figure 6 shows our best estimate of the rate coefficient for $^3CH_2 + OH$, along with the previous theoretical predictions of Wilson and Balint-Kurti[96] and Xia et al.[29] Our rate coefficient is in excellent agreement with that of ref 96, differing by less than 15% for 1000−2500 K, and is approximately a factor of 2 smaller than that of ref 29 over the same temperature range.

The rate for direct abstraction on the triplet surface has not been measured experimentally, making a theoretical determination necessary for interpreting related experimental results. As discussed in the next section, channel 1h becomes the dominant pathway for reaction 1 for temperatures above ∼1750 K.

IV.B. $CH_3 + OH$ Bimolecular Reaction. Pressure dependent rate coefficients were computed using the master equation approach discussed in section III. Figure 7 presents falloff curves for reaction 1 in He at 298 K along with several experimental results.[5−7,10] Good agreement is obtained using the exponential down model for the energy transfer function (eq 8), although our high-pressure limit is significantly lower than that of ref 10, as discussed above.

Only one of the sets of experimental results[7] shown in Figure 7 includes pressures less than 10 Torr and shows a discernible falloff behavior at room temperature, and our calculated low-pressure limit (4.2×10^{-11} cm^3 $molecule^{-1}$ s^{-1}) agrees well with their estimated range for this value ($(4.6-5.0) \times 10^{-11}$ cm^3 $molecule^{-1}$ s^{-1}). The experimental data indicate no significant pressure dependence above ∼10 Torr, whereas our calculation predicts falloff behavior up to ∼1000 Torr, although the predicted falloff is small and is similar in magnitude to the experimental uncertainties.

Next, we consider the sensitivity of the predicted falloff behavior to changes in the saddle point energies and in the thermochemistry of channel 1b. Lowering the saddle point barriers by 1 kcal/mol for channels 1c−1e or for channel 1b increased the low-pressure limit to 4.7×10^{-11} or 5.0×10^{-11} cm^3 $molecule^{-1}$ s^{-1}, respectively. Using the theoretical value for the 1b channel energy (0.03 kcal/mol relative to $CH_3 + OH$) had a more significant effect, resulting in a low-pressure limit of 5.2×10^{-11} cm^3 $molecule^{-1}$ s^{-1}. The effects of these changes

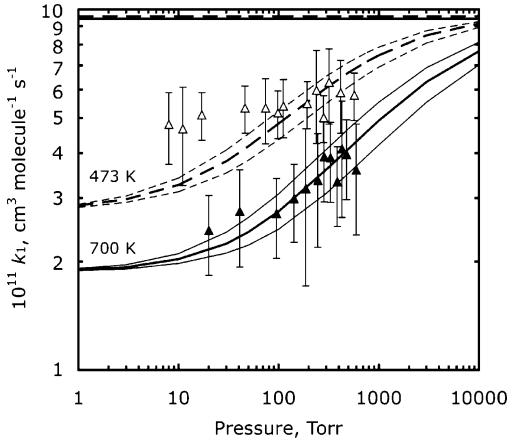

Figure 8. Falloff curves for the CH_3 + OH bimolecular reaction at 473 (dashed line) and 700 K (solid line) in He. The high-pressure limits are shown as horizontal lines. The effect of adjusting the energy transfer parameters by ±20% is indicated by thin lines. The experimental results of De Avillez Pereira et al.[6] are shown as triangles, where open and filled symbols indicate 473 and 700 K, respectively.

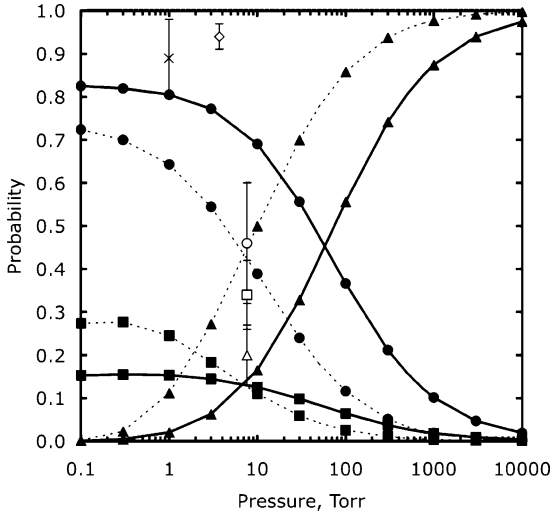

Figure 9. Branching fractions for the CH_3 + OH reaction for the products: CH_3OH (filled triangles), $^1CH_2$ + H_2O (filled circles), and H_2 + products (filled squares) at 298 (dotted lines) and 610 K (solid lines) in He. Also shown are the 298 K experimental $^1CH_2$ + H_2O product branching fractions of Deters et al.[7] (x) and Fockenberg et al.[18] (open diamond) and the 610 K product branching fractions of ref 18 for $^1CH_2$ + H_2O (open circle), CH_3OH (open triangle), and H_2 + products (open square).

on the computed rate coefficients are shown in Figure 7 and are of the same order as typical errors for statistical rate theories.

Falloff curves for reaction 1 at 473 and 700 K are presented in Figure 8, where they are shown to agree well with the experimental data of De Avillez Pereira et al.[6] These experimental falloff data were previously[6] used to obtain extrapolated estimates for k_1^∞, and the resulting values showed significant negative temperature dependence. The recommended values of ref 8 were largely based on those from ref 6. The present theoretical predictions fit the falloff data well, but our high-pressure limit is only very weakly dependent on temperature; i.e., we predict significantly more falloff at 473 and 700 K than was assumed in ref 6. This discrepancy highlights the uncertainties that can occur when extrapolating from experimental data obtained over a limited pressure range, as well as the usefulness of accurate theoretical models in interpreting these data.

The sensitivity of the computed rate coefficients to variations in $\langle\Delta E_d\rangle$ is also shown in Figure 8. The parameters α and γ in eq 8 were adjusted by ±20%, resulting in changes of less than 15% in the predicted rate coefficient.

Figure 9 presents product branching fractions, defined by

$$P_i = k_i/k_1 \qquad (11)$$

where *i* labels the channels, along with two sets of experimental measurements.[7,18]

The predicted value of P_{1b} at 298 K and 1−3 Torr (∼0.6) is somewhat lower than the range of the experimental determinations[7,18] (0.8−1.0). At 610 K and 8 Torr, however, the present calculation for P_{1b} (0.7) overestimates the importance of channel 1b relative to the measurement of Fockenberg et al.[18] (0.3−0.6). Reasonable adjustments to the energy of SP1 (±1 kcal/mol) change the predicted value of P_{1b} by ∼0.1, but the effect is in the same direction for both temperatures and does not therefore improve the overall agreement of the predicted and experimental results.

The theoretical prediction for $P_{H_2} \equiv P_{1c} + P_{1d} + P_{1e}$ at 610 K and 8 Torr is 0.1, which is lower than the experimental result[18] of 0.3−0.4. Adjusting all three H_2 saddle point energies downward by 1 kcal/mol increases the theoretical prediction of this value to 0.2 and reduces P_{1b} at the same conditions to 0.6, which is in better agreement with the experiment results. However, this adjustment also results in a lower theoretical prediction for P_{1b} at room temperature, which agrees less well with experiment.

Using the theoretical prediction for enthalpy of reaction 1b increases P_{1b} to ∼0.8 for both sets of experimental conditions, which results in poor agreement at 610 K at 8 Torr, and decreases P_{H_2} somewhat. None of these adjustments results in qualitatively better agreement between theory and the available experimental results, and we therefore restrict our attention to the unadjusted results in the remainder of this section.

The experiments of Grotheer and co-workers[9] indicated that stabilization (1a) was nearly the exclusive decay mechanism at low pressures (0.2−7 Torr) and 298 and 410 K, whereas the present theoretical results predict that channel 1a becomes the dominant product only at much higher pressures (∼100 Torr) as well as significant contributions from the H_2 product channels at low pressures. In experiments[11] at 700 K and 0.4 Torr, the formation of H_2 was observed, although the reported value for P_{H_2} (0.5) is much higher than the value predicted here (0.1). Grotheer et al.[11] measured falloff for reaction 1 under conditions where channel 1b was suppressed at 300 and 480 K and 0.2−7 Torr. If we consider only the stabilization channel 1a and repeat our master equation simulations, we find that we cannot achieve good agreement with the experimental results of ref 11 unless very large values for $\langle\Delta E_d\rangle$ (600−900 cm^{-1}) are used.

Next, we consider the CH_3 + OH bimolecular reaction in Ar and Kr at elevated temperatures. The present predicted rate coefficients are plotted in Figure 10 at 200 and 760 Torr for the bath gas Ar. Calculated total rate coefficients and product branching fractions for the bath gas Kr differed by less than 1% from those obtained for Ar. Also shown in Figure 10 are the experimental results of Bott and Cohen[15] (760 Torr Ar), Krasnoperov and Michael[16] (100−1100 Torr Kr), and Srinivasan et al.[17] (200−750 Torr Kr). A detailed comparison of the present theoretical results and the most recent experimental study is given in the companion paper.[17] Overall, the predicted rate coefficients agree well with the experimental results. The negative temperature dependence observed in k_1 at temperatures up to ∼1300 K can be attributed largely to increased falloff for the stabilization reaction 1a. The positive temperature depen-

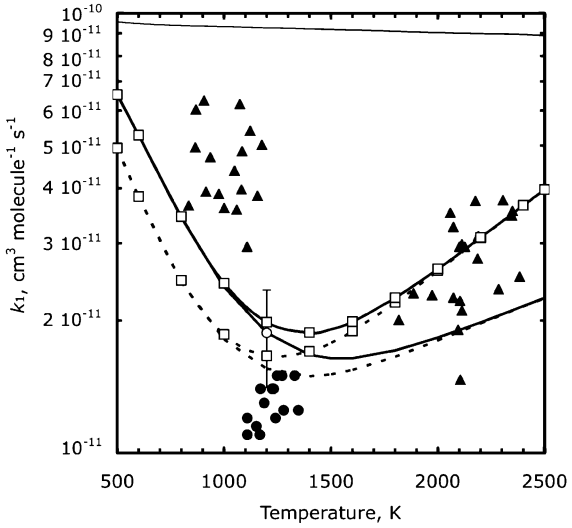

Figure 10. Rate coefficient for the CH_3 + OH reaction in Ar at 200 (dotted line) and 760 Torr (solid line), with (squares), and without (no symbols) including abstraction on the triplet surface (channel 1h). The high-pressure limiting rate coefficient (excluding channel 1h) is shown as a thin line. The experimental results of Bott and Cohen[15] (open circle), Krasnoperov and Michael[16] (triangles), and Srinivasan et al.[17] (filled circles) are also shown.

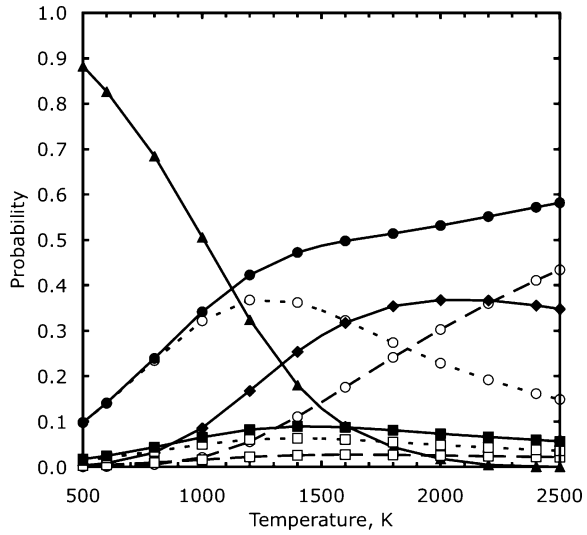

Figure 11. Branching fractions for the CH_3 + OH reaction for the products: CH_3OH (triangles); $^1CH_2 + H_2O$ (open circles with dotted lines), $^3CH_2 + H_2O$ (open circles with dashed lines), and their total (filled circles); H + CH_2OH (diamonds); H_2 + *cis*-HCOH (open squares with dotted lines), H_2 + *trans*-HCOH (open squares with dashed lines), and their total (filled squares) at 1 atm.

dence above ~1500 K is due in part to the increasing importance of the direct abstraction on the triplet surface (1h).

Product branching ratios for reaction 1 at 1 atm Ar are shown in Figure 11. The formation of CH_3OH dominates until ~1100 K, and the H_2O channels dominate at higher temperatures. Both the addition/elimination pathway for the formation of $^1CH_2$ + H_2O (1b) and the direct abstraction on the triplet surface (1h) are important product channels at high temperatures, with the direct abstraction becoming the dominant channel at ~1750 K. The H + CH_2OH channel is also important at elevated temperatures (>1000 K), whereas H + CH_3O is less than 1% of the total product formed over the entire temperature range. Less than 10% of the total product formed is H_2 + HCOH, with *trans*-HCOH forming twice as often as *cis*-HCOH. H_2CO is not a significant product of reaction 1 at these conditions,

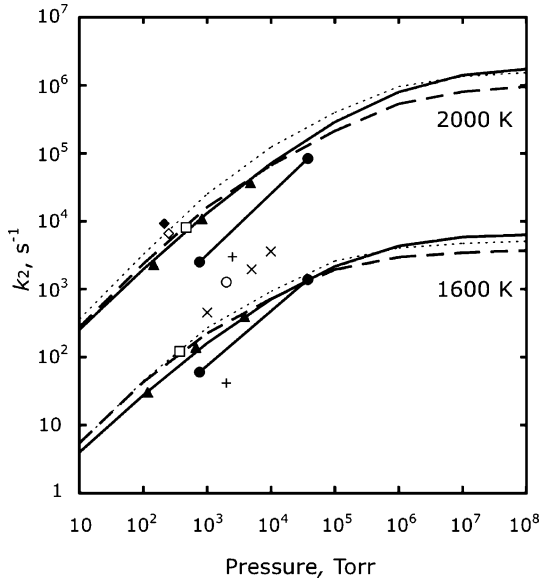

Figure 12. Falloff curves for CH_3OH decomposition in Ar (solid lines) at 1600 and 2000 K. Also shown are the experimental determinations of Bowman et al.[26] (+), Tsuboi et al.[23] (x, 1600 K only), Spindler et al.[25] (filled triangles), Cribb et al.[21] (open diamond, 2000 K only), Hidaka et al.[24] (open circle, 1600 K only), Cribb et al.[22] (filled diamond, 2000 K only), and Koike et al.[19] (open squares) and the recommended values of Held and Dryer[98] (dotted line) and Baulch et al.[8] (dashed line). The previous theoretical results of Xia et al.[29] are shown as filled circles.

although one would expect H_2CO to form quickly from HCOH as a secondary process.

Master equation simulations were carried out to estimate an upper limit on the effect of incorporating intersystem crossing in channel 1b, as discussed in section IV.A. These results suggest that intersystem crossing has a negligible effect on the kinetics of reaction 1 at elevated temperatures. At room temperature, the incorporation of intersystem crossing may increase P_{1b} by as much as ~0.15 at pressures up to 10 Torr, resulting in somewhat better agreement with the experimental determinations[7,18] discussed above, with both P_{H_2} and P_{1a} correspondingly reduced.

Analytic expressions for the pressure dependent rate coefficients for reaction 1 are given in the appendix.

IV.C. Methanol Decomposition. Pressure dependent rate coefficients were computed for the thermal dissociation of methanol using master equation simulations, as discussed in section III. Figure 12 presents predicted falloff for CH_3OH decomposition in Ar, along with several previous theoretical[29] and experimental[19,21−26] results. Also shown are two recent sets of recommended values.[8,98] The predicted rate coefficients are within 15% of the experimental results of Spindler et al.[25] and are ~20% lower than the results of Koike et al.[19] and Cribb et al.[21,22] The experimental results of Tsuboi et al.[23] and Hidaka et al.[24] are significantly higher (by factors of 3−5) than those obtained in the present work. The theoretical results of Xia et al.[29] are 2−4 times lower than the present predicted values for k_2 at 1 atm. In the high-pressure limit, the present predicted results agree well with the recommendations of Held and Dryer[98] and are somewhat higher than those of Baulch et al.[8]

Figure 13 presents several experimentally measured,[16,17,19,20,22] or extrapolated[23,25] low-pressure limit rate coefficients for CH_3-OH → CH_3 + OH, along with the present predicted values at 200 and 760 Torr. There is little pressure dependence in the present values for k_2 for pressures less than ~5 atm, as suggested experimentally. The predicted values are lower than those

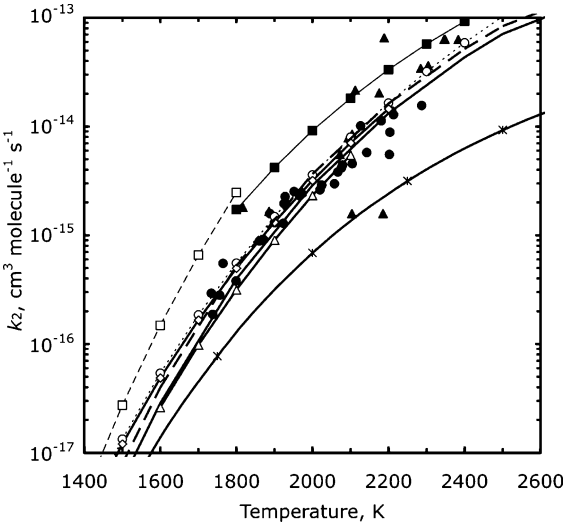

Figure 13. Decomposition rates for CH_3OH in Ar at 200 (dashed line) and 760 Torr (solid line). Also shown are the experimental determinations of Tsuboi et al.[23] (open squares), Spindler et al.[25] (open triangles), Dombrowsky et al.[20] (open diamonds), Cribb et al.[21] (filled squares), Koike et al.[19] (open circles), Krasnoperov and Michael[16] (filled triangles), and Srinivasan et al.[17] (filled circles). The previous theoretical result of Xia et al.[29] at 760 Torr are also shown (*).

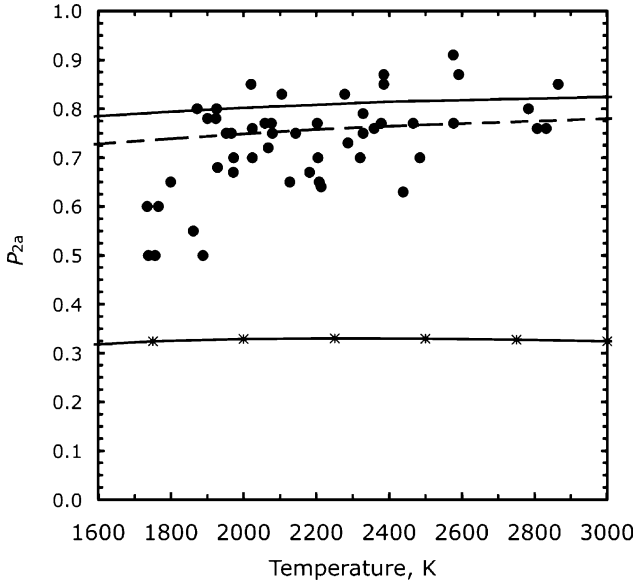

Figure 14. Branching fraction for the formation of $CH_3 + OH$ from the decomposition of methanol in Ar at 200 (dashed line) and 760 Torr (solid line). Also shown are the experimental determinations of Srinivasan et al.[17] (circles) and the previous theoretical results of Xia et al.[29] at 760 Torr (*).

reported by Cribb et al.[22] and Tsuboi et al.[23] and are in excellent agreement with the remaining experimental studies, including the recent set of direct measurements made by Michael and coworkers.[16,17] Also shown in Figure 13 are the results of the previous theoretical study of Xia et al.[29] at 1 atm, which are 30−80% lower than the present theoretical predictions.

$CH_3 + OH$ has long been recognized experimentally as the dominant product of reaction 2, with branching fractions for this channel variously measured or estimated as 80−85%,[25] 70−80%,[24] >75%,[20] 76%,[21,22] and 94%.[16] In the companion paper, Srinivasan et al.[17] measured the product branching for reaction 2 directly, and their experimental results range from 50−90% with an average of 73%, as shown in Figure 14. Also shown are the present predicted values for P_{2a} at 200 and 760 Torr. There is significant scatter in the experimental data due to the relative insensitivity of P_{2a} on the overall measured rate for decomposition, but the agreement with the present theoretical results is excellent. Both theory and experiment predict a slight temperature dependence in the branching fraction, with the relative formation of $CH_3 + OH$ increasing with temperature.

The remainder of the total rate for reaction 2 is typically attributed to the formation of $CH_2OH + H$, although Dombrowsky et al.[20] suggested $^1CH_2 + H_2O$ as the second most important product. The present theoretical results support the view of Dombrowsky et al. and predict $^1CH_2 + H_2O$ to be the second most important product (15−20%), except at very low temperatures (<500 K) where the formation of $H_2 + HCOH$ becomes important. At temperatures relevant to combustion, the present theoretical predictions show only minor contributions from $H_2 + HCOH$ (<3%), $H + CH_2OH$ (<1%), $H_2 + H_2CO$ (≪1%), and $H + CH_3O$ (≪1%). Previously, at 1500−2500 K and 1 atm, Xia et al.[29] predicted product branching fractions for reaction 2 of 33%, 52%, and 14% for $CH_3 + OH$, $^1CH_2 + H_2O$, and $H_2 + HCOH$, respectively.

Master equation simulations for reaction 2 were carried out to estimate an upper limit on the effect of incorporating intersystem crossing in channel 2b, as discussed in section IV.A. These results suggest that intersystem crossing may lower P_{2a} by no more than 0.05 at 1600−3000 K, with the effect most significant at lower temperatures and pressures.

Analytic expressions for the pressure dependent rate coefficients for reaction 2 are given in the appendix.

V. Conclusions

A theoretical study of the kinetics of the $CH_3 + OH$ bimolecular reaction and the decomposition of methanol has been performed for a wide range of temperatures and pressures, including those relevant to combustion. Rate coefficients were determined using a combination of ab initio calculations, variational transition state theory, and master equation simulations, and detailed comparisons were made with available experimental and previous theoretical results.

A composite potential energy surface for CH_3OH was constructed using channel energies obtained from the Active Thermochemical Tables (ATcT) along with the results of high-level electronic structure calculations. The channel energy of $^1CH_2 + H_2O$ is nearly thermoneutral with $CH_3 + OH$, and several recent high-level electronic structure calculations have predicted both endothermic and exothermic reaction enthalpies for $CH_3 + OH \rightarrow {}^1CH_2 + H_2O$. The theoretical predictions vary by ∼2 kcal/mol, and these differences can have an important effect of the overall kinetics of reactions 1 and 2. The use of ATcT channel energies with small uncertainties (typically, less than 0.1 kcal/mol) obviates the need for higher level calculations to resolve this theoretical ambiguity.

The transition state for the $^1CH_2 + H_2O$ channel was treated using a microcanonical two transition state model. Good agreement was obtained between the predicted values and the experimental measurements for the capture rate at 300−500 K. The importance of coupling the microcanonical fluxes associated with the inner and outer transition states was demonstrated. Coupling the two transition states canonically was shown to overestimate the rate coefficient at room temperature by more than a factor of 5. Neglecting the outer transition state was also shown to be a poor approximation for temperatures as high as 1500 K.

The barrierless transition states for $CH_3 + OH$, $CH_3O + H$, and $CH_2OH + H$ were treated using variable reaction coordinate transition state theory (VRC-TST) and multireference ab initio

methods to directly evaluate the interaction potential. The VRC-TST prediction for the capture rate coefficient for $CH_3 + OH$ was found to be in excellent agreement with the majority of experimental room-temperature determinations, differing from them by only ~4−30%. This level of accuracy is similar to that obtained recently for hydrocarbon radical−radical reactions using ab initio VRC-TST, further validating the method.

The capture rate coefficient for $CH_3 + OH$ was predicted to be nearly independent of temperature, and the apparent discrepancy between the present prediction and an experimental study demonstrating significant temperature dependence up to 700 K was suggested to be a result of falloff in the experimental results.

Predicted rate coefficients for $CH_3 + OH$ at 200−1000 Torr were found to be in good agreement with recent shock tube determinations, including those from a companion study by Michael and co-workers,[17] differing by less than a factor of 2. The increased importance of the direct abstraction on the triplet surface at temperatures above 1200 K was shown to result in V-shaped constant pressure rate coefficients, as observed experimentally. The major products of reaction 1 were predicted to be sensitive to temperature and pressure, and several products were found to be significant, including CH_3OH, $CH_2 + H_2O$, $H + CH_2OH$, and $H_2 + HCOH$.

Low-pressure rate coefficients for methanol decomposition were presented and were shown to be in good agreement with the majority of experimental results, including the direct measurements of Srinivasan and Michael reported in a companion paper.[17] Rate coefficients for reaction 2 were found to be fairly insensitive to pressure up to ~5 atm, and predicted falloff for reaction 2 was in good agreement with several experimental and recommended results. The major product of reaction 2 under combustion conditions was confirmed to be $CH_3 + OH$ (~80%). The second most important product at

TABLE 4: Modified Troe Parameters for the $CH_3 + OH$ Reaction ($T = 300-3000$ K; $P = 1-10^5$ Torr)

product	A[a]	n	E (K)	A' [a]	n'	E' (K)
CH_3OH[b]	6.487×10^{-22}	−9.880	7544	1.684×10^{-26}	−6.250	1433
$^1CH_2 + H_2O$	4.642×10^{-11}	−1.172	132.0	2.850×10^{-14}	2.127	547.8
H_2 + *trans*-HCOH	1.018×10^{-11}	−1.875	23.44	5.330×10^{-13}	0.524	767.6
H_2 + *cis*-HCOH	1.298×10^{-12}	--1.501	89.82	1.158×10^{-13}	1.000	617.1
$H_2 + H_2CO$	2.070×10^{-13}	--1.234	−19.57	2.453×10^{-8}	−4.484	9188
$H + CH_2OH$	3.202×10^{-12}	0.996	1606			
$H + CH_3O$	6.495×10^{-13}	1.014	6013			

product	A'' [c]	n''	E'' (K)
CH_3OH[b]	9.305×10^{-11}	−0.018	−16.74
$^1CH_2 + H_2O$	1.117×10^{7}	4.096	−625.0
H_2 + *trans*-HCOH	7.903×10^{4}	6.225	−1573
H_2 + *cis*-HCOH	3.162×10^{4}	6.406	−1250
$H_2 + H_2CO$	2.617×10^{3}	6.721	−1521
$H + CH_2OH$	1.500×10^{7}	5.009	949.4
$H + CH_3O$	1.995	18.59	−13.66

product	a	b	c	d
CH_3OH[b]	0.1855	155.8	1675	4531
$^1CH_2 + H_2O$	0.4863	321.4	30000	2804
H_2 + *trans*-HCOH	0.5312	235.3	16882	2812
H_2 + *cis*-HCOH	0.4375	117.2	16876	2813
$H_2 + H_2CO$	0.5000	22122	174.9	3047
$H + CH_2OH$	0.8622	9321	361.8	3125
$H + CH_3O$	0.2500	26220	937.5	3984

[a] A and A' are given in cm^6 $molecule^{-2}$ s^{-1} for CH_3OH and cm^3 $molecule^{-1}$ s^{-1} otherwise. [b] Fit for $T = 300-2000$ K. [c] A'' is given in cm^3 $molecule^{-1}$ s^{-1} for CH_3OH and s^{-1} otherwise.

TABLE 5: Modified Troe Parameters for CH_3OH Decomposition ($T = 1000-3000$ K; $P = 100-10^5$ Torr)

product	A (cm^3 $molecule^{-1}$ s^{-1})	n	E (K)	A' (cm^3 $molecule^{-1}$ s^{-1})	n'	E'(K)
$CH_3 + OH$	1.161×10^{5}	−9.750	53086	4.531	−6.999	47656
$^1CH_2 + H_2O$	8.030×10^{4}	−10.20	52454	6.245	−6.577	48007
H_2 + *trans*-HCOH	4.954×10^{4}	−11.26	47912	7.016×10^{6}	−12.67	54196
H_2 + *cis*-HCOH	8.729×10^{6}	−4.375	39670	3.463×10^{2}	−9.980	50567
$H + CH_2OH$	1.007×10^{1}	−7.527	53117	2.285	−7.095	55202

product	A'' (s^{-1})	n''	E'' (K)
$CH_3 + OH$	6.251×10^{16}	−0.6148	46573
$^1CH_2 + H_2O$	9.443×10^{15}	−1.017	46156
H_2 + *trans*-HCOH	1.933×10^{12}	1.650	42643
H_2 + *cis*-HCOH	2.405×10^{12}	1.612	44273
$H + CH_2OH$	2.383×10^{10}	5.038	42510

product	a	b	c	d
$CH_3 + OH$	0.7656	1910	59.51	9374
$^1CH_2 + H_2O$	0.9922	943.0	47310	47110
H_2 + *trans*-HCOH	0.8423	235.0	1953	18165
H_2 + *cis*-HCOH	0.7812	251.8	12500	31248
$H + CH_2OH$	0.6843	37049	41493	3980

elevated temperatures was shown to be $CH_2 + H_2O$ (~20%), as suggested by Dombrowsky et al.,[20] and not $CH_2OH + H$, as has been suggested elsewhere.

The present theoretical predictions for reactions 1 and 2 provide a consistent picture of the kinetics for these reactions over a wide range of temperatures and pressures. When available and unambiguous, experimental results are generally in good agreement with the present theoretical ones, and when the experimental results are contradictory, the present results may be used for clarification. Furthermore, the present theoretical results allow for the characterization of reactions 1 and 2 at temperatures and pressures where direct measurements are difficult or not possible. The present study makes use of a variety of theoretical methods and techniques, which have been developed and refined for several decades, and the present study confirms the usefulness of these methods in generating quantitative rates for multichannel reactions. These methods may be applied to less well characterized systems with confidence.

Acknowledgment. We thank Brian Serve and De-Cai Fang for their helpful contributions to early stages of this work. This work was performed under the auspices of the Office of Basic Energy Sciences, Division of Chemical Sciences, Geosciences, and Biosciences, U.S. Department of Energy, under contract number DE-AC02-06CH11357.

Supporting Information Available: QCISD(T) energies and B3LYP/6-311++G** geometries, vibrational frequencies, and rotational constants of the product fragments and stationary points on the CH_3OH potential energy surface. This material is available free of charge via the Internet at http://pubs.acs.org.

Appendix: Analytic Expressions for the Pressure Dependent Rate Coefficients and Estimates of the Computed Uncertainties

Rate coefficients for the $CH_3 + OH$ reaction in Ar at $1-10^5$ Torr and 300−3000 K for each product channel i were fit to[32]

$$k_i = \frac{k_i^\infty k_i^0[\mathrm{M}]}{k_i^\infty + k_i^0[\mathrm{M}]} F_i \qquad (i = 1\mathrm{a}) \tag{12}$$

$$k_i = \frac{k_i^\infty k_i^0}{k_i^\infty + k_i^0[\mathrm{M}]} F_i \qquad (i = 1\mathrm{b}-1\mathrm{g}) \tag{13}$$

where

$$\log F_i = \frac{\log F_i^c}{1 + [\log(k_i^0[\mathrm{M}]/k_i^\infty)/N_i]^2} \tag{14}$$

$$N_i = 0.75 - 1.27 \log F_i^c \tag{15}$$

$$F_i^c = a \exp(-b/T) + (1 - a) \exp(-c/T) + \exp(-T/d) \tag{16}$$

[M] is the concentration of the bath gas, and k_i^∞ and k_i^0 are parametrized as modified Arrhenius expressions:

$$k_i^0 = A(T/300\ \mathrm{K})^n \exp(-E/T) + A'(T/300\ \mathrm{K})^{n'} \exp(-E'/T) \tag{17}$$

$$k_i^\infty = A''(T/300\ \mathrm{K})^{n''} \exp(-E''/T) \tag{18}$$

Maximum fitting errors were less than 20%, and average fitting errors were 3−5%. Note that k_i^∞ and k_i^0 are used as fitting parameters, and due to the finite range of pressures considered during the fit, these expressions do not necessarily represent the high- and low-pressure limits, respectively. Fitting parameters are summarized in Table 4.

Rate coefficients for CH_3OH decomposition in Ar at $100-10^5$ Torr and 1000−3000 K for the products $CH_3 + OH$, $^1CH_2 + H_2O$, $H_2 + HCOH$, and $H + CH_2OH$ were fit to eq 12 with typical fitting errors of 3−10%. Fitting parameters are summarized in Table 5.

An evaluation of the uncertainties associated with the theoretical rate coefficients reported in Tables 3−5 requires the consideration of several sources of error, and the quantification of the contribution of each of these sources of error to the overall uncertainty for each rate coefficient requires extensive systematic studies beyond the scope of the present work. In fact, one goal of the present study is to compare the results of our best theoretical models with experimental results for reactions 1 and 2, which have been fairly well characterized experimentally. On the basis of the present evaluations and on previous work, we estimate 2σ uncertainty factors of 1.5−2 for the theoretical predictions in Tables 4 and 5. The uncertainty in the barrierless capture rate coefficients computed using VRC-TST is much smaller and is likely only ~20−30%. We estimate uncertainties for the remaining rate coefficients given in Table 3 to be 30−40% for temperatures above 1000 K, with the uncertainty increasing at lower temperatures.

References and Notes

(1) Minet, R. G. *Science* **1967**, *157*, 1373. Reed, T. B.; Lerner, R. M. *Science* **1973**, *182*, 1299. Olah, G. A. *Angew. Chem., Int. Ed.* **2005**, *44*, 2636.
(2) Moreira, J. R.; Goldemberg, J. *Energy Policy* **1999**, *27*, 229.
(3) Sworski, T. J.; Hochanadel, C. J.; Ogren, P. J. *J. Phys. Chem.* **1980**, *84*, 129.
(4) Anastasi, C.; Beverton, S.; Ellermann, T.; Pagsberg, P. *J. Chem. Soc., Faraday Trans.* **1991**, *87*, 2325.
(5) Hughes, K. J.; Pereira, A. R.; Pilling, M. J. *Ber. Bunsen-Ges. Phys. Chem.* **1992**, *96*, 1352.
(6) De Avillez Pereira, R.; Baulch, D. L.; Pilling, M. J.; Robertson, S. H.; Zeng, G. *J. Phys. Chem. A* **1997**, *101*, 9681; de Avillez Pereira, R. *J. Phys. Chem. A* **2005**, *110*, 2079. Pilling, M. J. *J. Phys. Chem. A* **2005**, *110*, 2080.
(7) Deters, R.; Otting, M.; Wagner, H. G.; Temps, F.; László, B.; Dóbé, S.; Bérces, T. *Ber. Bunsen-Ges. Phys. Chem.* **1998**, *102*, 58.
(8) Baulch, D. L.; Bowman, C. T.; Cobos, C. J.; Cox, R. A.; Just, Th.; Kerr, J. A.; Pilling, M. J.; Stocker, D.; Troe, J.; Tsang, W.; Walker, R. W.; Warnatz, *J. Phys. Chem. Ref. Data* **2005**, *34*, 757.
(9) Oser, H.; Stothard, N. D.; Humpfer, R.; Grotheer, H. H. *J. Phys. Chem.* **1992**, *96*, 5359.
(10) Fagerström, K.; Lund, A.; Mahmoud, G.; Jadkowski, J. T.; Ratajczak, E. *Chem. Phys. Lett.* **1993**, *204*, 226.
(11) Oser, H.; Stothard, N. D.; Humpfer, R.; Grotheer, H. H.; Just, T. *Symp. (Int.) Combust.* **1992**, *24*, 597.
(12) Humpfer, R.; Oser, H.; Grotheer, H. H.; Just, T. *Symp. (Int.) Combust.* **1994**, *25*, 721.
(13) Humpfer, R.; Oser, H.; Grotheer, H.-H. *Int. J. Chem. Kinet.* **1995**, *27*, 577.
(14) Fagerström, K.; Lund, A.; Mahmoud, G.; Jadkowski, J. T.; Ratajczak, E. *Chem. Phys. Lett.* **1994**, *224*, 43.
(15) Bott, J. F.; Cohen, N. *Int. J. Chem. Kinet.* **1991**, *23*, 1017.
(16) Krasnoperov, L. N.; Michael, J. V. *J. Phys. Chem. A* **2004**, *108*, 8317.
(17) Srinivasan, N. K.; Su, M.-C.; Michael, J. V. *J. Phys. Chem. A* **2007**, *111*, 3951.
(18) Fockenberg, C.; Weston, R. E.; Muckerman, J. T. *J. Phys. Chem. B* **2005**, *109*, 8415.
(19) Koike, T.; Kudo, I.; Yamada, H. *Int. J. Chem. Kinet.* **2000**, *32*, 1.
(20) Dombrowsky, C.; Hoffman. A.; Klatt, M.; Wagner, H. G. *Ber. Bunsen-Ges. Phys. Chem.* **1991**, *95*, 1685.
(21) Cribb, P. H.; Dove, J. E.; Yamazaki, S. *Symp. (Int.) Combust.* **1984**, *20*, 779.

(22) Cribb, P. H.; Dove, J. E.; Yamazaki, S. *Combust. Flame* **1992**, *88*, 169.
(23) Tsuboi, T.; Masataka, K.; Kikuch, S.; Hashimoto, K. *Jpn. J. Appl. Phys.* **1981**, *20*, 985.
(24) Hidaka, Y.; Oki, T.; Kawano, H.; Higashihara, T. *J. Phys. Chem.* **1989**, *93*, 7134.
(25) Spindler, K.; Wagner, H. Gg. *Ber. Bunsen-Ges. Phys. Chem.* **1982**, *86*, 2.
(26) Bowman, C. T. *Combust. Flame* **1975**, *25*, 343.
(27) Aronowitz, D.; Naegell, D. W.; Glassman, I. *J. Phys. Chem.* **1977**, *81*, 2555.
(28) Cathonnet, M.; Boettner, J.-C.; James, H. *J. Chim. Phys.* **1979**, *76*, 183.
(29) Xia, W. S.; Zhu, R. S.; Lin, M. C.; Mebel, A. M. *Faraday Discuss.* **2001**, *119*, 191.
(30) Ing, W.-C.; Sheng, C. Y.; Bozzelli, J. W. *Fuel Process. Technol.* **2003**, *83*, 111.
(31) Jordan, M. J. T.; Smith, S. C.; Gilbert, R. G. *J. Phys. Chem.* **1991**, *95*, 8685.
(32) Troe, J. *J. Phys. Chem.* **1979**, *83*, 114.
(33) Troe, J. *Ber. Bunsen-Ges. Phys. Chem.* **1983**, *87*, 161.
(34) Gilbert, R. G.; Luther, K.; Troe, J. *Ber. Bunsen-Ges. Phys. Chem.* **1983**, *87*, 169.
(35) Miller, J. A.; Klippenstein, S. J.; Raffy, C. *J. Phys. Chem. A* **2002**, *106*, 4904.
(36) Miller, J. A.; Klippenstein, S. J. *Int. J. Chem. Kinet.* **2001**, *33*, 654.
(37) Ruscic, B.; Pinzon, R. E.; Morton, M. L.; von Laszewski, G.; Bittner, S.; Nijsure, S. G.; Amin, K. A.; Minkoff, M.; Wagner, A. F. *J. Phys. Chem. A* **2004**, *108*, 9979.
(38) Ruscic, B.; Pinzon, R. E.; von Laszewski, G.; Kodeboyina, D.; Burcat, A.; Leahy, D.; Montoya, D.; Wagner, A. F. *J. Phys. Conf. Ser.* **2005**, *16*, 56.
(39) Ruscic, B. Active Thermochemical Tables. In *2005 Yearbook of Science and Technology*; McGraw-Hill: New York, 2004; pp 3−7.
(40) Ruscic, B.; Pinzon, R. E.; Morton, M. L.; Srinivasan, N. K.; Su, M.-C.; Sutherland, J. W.; Michael, J. V. *J. Phys. Chem. A.* **2006**, *110*, 6592.
(41) Truhlar, D. G.; Garrett, B. C.; Klippenstein, S. J. *J. Phys. Chem.* **1996**, *100*, 12771.
(42) Dean, A. M.; Westmoreland, P. R. *Int. J. Chem. Kinet.* **1987**, *19*, 207.
(43) Klippenstein, S. J. *J. Chem. Phys.* **1992**, *96*, 367.
(44) Klippenstein, S. J. *J. Phys. Chem.* **1994**, *98*, 11459.
(45) Georgievskii, Y.; Klippenstein, S. J. *J. Chem. Phys.* **2003**, *118*, 5442.
(46) Harding, L. B.; Georgievskii, Y.; Klippenstein, S. J. *J. Phys. Chem. A* **2005**, *109*, 4646.
(47) Klippenstein, S. J.; Georgievskii, Y.; Harding, L. B. *Phys. Chem. Chem. Phys.* **2006**, *8*, 1133.
(48) Greenwald, E. E.; North, S. W.; Georgievskii, Y.; Klippenstein, S. J. *J. Phys. Chem. A* **2005**, *109*, 6031.
(49) Miller, W. H. *J. Chem. Phys.* **1976**, *65*, 2216.
(50) Ruscic, B.; Pinzon, R. E.; von Laszewski, G. Manuscript in preparation.
(51) Yu, H.-G.; Muckerman, J. T. *J. Phys. Chem. A* **2004**, *108*, 8615.
(52) Hack, W.; Wagner, H. G.; Wilms, A. *Ber. Bunsen-Ges. Phys. Chem.* **1988**, *92*, 620.
(53) Lee, R. J.; Ripley, F. M.; Miller J. A. *Chemkin Thermodynamic Data Base*; SANDIA Report 87-8215 UC4; Sandia National Laboratories: Livermore, CA, 1987.
(54) Ruscic, B.; Litorja, M.; Asher, R. L. *J. Phys. Chem. A* **1999**, *103*, 8625.
(55) Ruscic, B.; Feller, D.; Dixon, D. A.; Peterson, K. A.; Harding, L. B.; Asher, R. L.; Wagner, A. F. *J. Phys. Chem. A* **2001**, *105*, 1.
(56) Ruscic, B.; Wagner, A. F.; Harding, L. B.; Asher, R. L.; Feller, D.; Dixon, D. A.; Peterson, K. A.; Song, Y.; Qian, X.; Ng, C.-Y.; Liu, J.; Chen, W.; Schwenke, D. W. *J. Phys. Chem. A* **2002**, *106*, 2727.
(57) Ruscic, B.; Boggs, J. E.; Burcat, A.; Csaszar, A. G.; Demaison, J.; Janoschek, R.; Martin, J. M. L.; Morton, M. L.; Rossi, M. J.; Stanton, J. F.; Szalay, P. G.; Westmoreland, P. R.; Zabel, F.; Berces, T. *J. Phys. Chem. Ref. Data* **2005**, *34*, 573.
(58) Becke, A. D. *J. Chem. Phys.* **1993**, *98*, 5648. Lee, C.; Yang, W.; Parr, R. G. *Phys. Rev. B* **1998**, *37*, 785.
(59) Krishnan, R.; Binkley, J. S.; Seeger, R.; Pople, J. A. *J. Chem. Phys.* **1980**, *72*, 650. Clark, T.; Chadrasekhar, J.; Schleyer, P. v. R. *J. Comput. Chem.* **1993**, *4*, 294.
(60) Pople, J. A.; Head-Gordon, M.; Raghavachari, K. *J. Chem. Phys.* **1987**, *87*, 5968. Raghavachari, K.; Trucks, G. W.; Pople, J. A.; Head-Gordon, M. *Chem. Phys. Lett.* **1989**, *157*, 479.
(61) Martin, J. M. L.; Uzan, O. *Chem. Phys. Lett.* **1998**, *282*, 16.
(62) Dunning, T. H., Jr. *J. Chem. Phys.* **1989**, *90*, 1007.
(63) Lee, T. J.; Rendell, A. P.; Taylor, P. R. *J. Phys. Chem.* **1990**, *94*, 5463.
(64) Hill, E. L.; Van Vleck, J. H. *Phys. Rev.* **1923**, *32*, 250.
(65) Herzberg, G. *Spectra of Diatomic Molecules*; Van Nostrand: New York, 1967; p 232.
(66) Kendall, R. A.; Dunning, T. H., Jr.; Harrison, R. J. *J. Chem. Phys.* **1992**, *96*, 6796.
(67) Andersson, K.; Malmqvist, P.-A.; Roos, B. O. *J. Chem. Phys.* **1992**, *96*, 1218. Werner, H.-J. *Mol. Phys.* **1996**, *89*, 645. Celani, P.; Werner, H.-J. *J. Chem. Phys.* **2000**, *112*, 5546.
(68) Berning, A.; Schweizer, M.; Werner, H.-J.; Knowles, P. J.; Palmier, P. *Mol. Phys.* **2000**, *98*, 1823.
(69) Roos, B. O.; Andersson, K. *Chem. Phys. Lett.* **1995**, *245*, 215. Celani, P.; Werner, H.-J. *J. Chem. Phys.* **2003**, *119*, 5044.
(70) Frisch, M. J.; Trucks, G. W.; Schlegel, H. B.; Scuseria, G. E.; Robb, M. A.; Cheeseman, J. R.; Montgomery, J. A., Jr.; Vreven, T.; Kudin, K. N.; Burant, J. C.; Millam, J. M.; Iyengar, S. S.; Tomasi, J.; Barone, V.; Mennucci, B.; Cossi, M.; Scalmani, G.; Rega, N.; Petersson, G. A.; Nakatsuji, H.; Hada, M.; Ehara, M.; Toyota, K.; Fukuda, R.; Hasegawa, J.; Ishida, M.; Nakajima, T.; Honda, Y.; Kitao, O.; Nakai, H.; Klene, M.; Li, X.; Knox, J. E.; Hratchian, H. P.; Cross, J. B.; Bakken, V.; Adamo, C.; Jaramillo, J.; Gomperts, R.; Stratmann, R. E.; Yazyev, O.; Austin, A. J.; Cammi, R.; Pomelli, C.; Ochterski, J. W.; Ayala, P. Y.; Morokuma, K.; Voth, G. A.; Salvador, P.; Dannenberg, J. J.; Zakrzewski, V. G.; Dapprich, S.; Daniels, A. D.; Strain, M. C.; Farkas, O.; Malick, D. K.; Rabuck, A. D.; Raghavachari, K.; Foresman, J. B.; Ortiz, J. V.; Cui, Q.; Baboul, A. G.; Clifford, S.; Cioslowski, J.; Stefanov, B. B.; Liu, G.; Liashenko, A.; Piskorz, P.; Komaromi, I.; Martin, R. L.; Fox, D. J.; Keith, T.; Al-Laham, M. A.; Peng, C. Y.; Nanayakkara, A.; Challacombe, M.; Gill, P. M. W.; Johnson, B.; Chen, W.; Wong, M. W.; Gonzalez, C.; Pople, J. A. *Gaussian 98*, revision A.7; Gaussian, Inc.: Wallingford, CT, 2004.
(71) Werner, H.-J.; Knowles, P. J.; Schütz, M.; Lindh, R.; Celani, P.; Korona, T.; Rauhut, G.; Manby, F. R.; Amos, R. D.; Bernhardsson, A.; Berning, A.; Cooper, D. L.; Deegan, M. J. O.; Dobbyn, A. J.; Eckert, F.; Hampel, C.; Hetzer, G.; Lloyd, A. W.; McNicholas, S. J.; Meyer, W.; Mura, M. E.; Nicklass, A.; Palmieri, P.; Pitzer, R.; Schumann, U.; Stoll, H.; Stone A. J.; Tarroni, R.; Thorsteinsson, T. MOLPRO, Version 2002.3.
(72) VaReCoF, Georgievskii, Y.; Klippenstein, S. J. Sandia National Laboratories and Argonne National Laboratory, 2006.
(73) Wardlaw, D. M.; Marcus, R. A. *Chem. Phys. Lett.* **1984**, *110*, 230; *J. Chem. Phys.* **1985**, *83*, 3462; *J. Phys. Chem.* **1986**, *90*, 5838.
(74) Klippenstein, S. J.; Harding, L. B. *Phys. Chem. Chem. Phys.* **1999**, *1*, 989.
(75) Georgievskii, Y.; Klippenstein, S. J. *J. Phys. Chem. A* **2003**, *107*, 9776.
(76) Medvedev, D. M.; Harding, L. B.; Gray, S. K. *Mol. Phys.* **2006**, *104*, 73.
(77) Taatjes, C. A.; Klippenstein, S. J. *J. Phys. Chem. A.* **2001**, *105*, 8567.
(78) Johnston, H. S.; Heicklen, J. *J. Phys. Chem.* **1962**, *66*, 532.
(79) Jackels, C. F.; Gu, Z.; Truhlar, D. G. *J. Chem. Phys.* **1995**, *102*, 3188.
(80) Nguyen, K. A.; Jackels, C. F.; Truhlar, D. G. *J. Chem. Phys.* **1996**, *104*, 6491.
(81) Chuang, Y.-Y.; Truhlar, D. G. *J. Phys. Chem. A* **1998**, *102*, 242.
(82) Corchado, J. C.; Chuang, Y.-Y.; Fast, P. L.; Hu, W.-P.; Liu, Y.-P.; Lynch, G. C.; Nguyen, K. A.; Jackels, C. F.; Fernandez Ramos, A.; Ellingson, B. A.; Lynch, B. J.; Melissas, V. S.; Villà, J.; Rossi, I.; Coitiño, E. L.; Pu, J.; Albu, T. V.; Steckler, R.; Garrett, B. C.; Isaacson, A. D.; Truhlar, D. G. POLYRATE−version 9.4; University of Minnesota: Minneapolis, 2005.
(83) Rai, S. N.; Truhlar, D. G. *J. Chem. Phys.* **1983**, *79*, 6046.
(84) Klippenstein, S. J.; Khundkar, L. R.; Zewail, A. H.; Marcus, R. A. *J. Chem. Phys.* **1988**, *89*, 4761.
(85) Klippenstein, S. J.; Wagner, A. F.; Dunbar, R. C.; Wardlaw, D. M.; Robertson, S. H.; Miller, J. A. VariFlex, version 1.14m; Argonne National Laboratory: Argonne, IL, 2006.
(86) Klippenstein, S. J.; Miller, J. A. *J. Phys. Chem. A* **2002**, *106*, 9267.
(87) Miller, J. A.; Klippenstein, S. J. *J. Phys. Chem. A* **2006**, *110*, 10528.
(88) Miller, J. A.; Klippenstein, S. J. *J. Phys. Chem. A* **2003**, *107*, 2680.
(89) Senosiain, J. P.; Klippenstein, S. J.; Miller, J. A. *J. Phys. Chem. A.* **2005**, *109*, 6045.
(90) Hirschfelder, J. O.; Curtiss, C. F.; Bird, R. B. *Molecular Theory of Gases and Liquids*; Wiley: New York, 1954; pp 1110, 1212.
(91) Gutsche, G. J.; Lawrance, W. D.; Staker, W. S.; King, K. D. *J. Phys. Chem.* **1995**, *99*, 11876.
(92) Carstensen, H.-H.; Wagner, H. G. *Ber. Bunsen-Ges. Phys. Chem.* **1995**, *99*, 1539.
(93) Hayes, F.; Lawrance, W. D.; Staker, W. S.; King, K. D. *J. Phys. Chem.* **1996**, *100*, 11314.
(94) Bley, U.; Temps, F. *J. Chem. Phys.* **1993**, *98*, 1058.
(95) Dóbé, S.; Bérces, T.; Szilagyi, I. *J. Chem. Soc., Faraday Trans.* **1991**, *87*, 2331.
(96) Wilson, C.; Balint-Kurti, G. G. *J. Phys. Chem. A* **1998**, *102*, 1625.

(97) Lu, D.-H.; Truong, T. N.; Melissas, V. S.; Lynch, G. C.; Liu, Y.-P.; Garrett, B. C.; Steckler, R.; Isaacson, A. D.; Rai, S. N.; Hancock, G.; Lauderdale, J. G.; Joseph, T.; Truhlar, D. G. *Comput. Phys. Commun.* **1992**, *71*, 235. Liu, Y.-P.; Lynch, G. C.; Truong, T. N.; Lu, D.-H.; Truhlar, D. G. *J. Am. Chem. Soc.* **1993**, *115*, 2408.

(98) Held, T. J.; Dryer, F. L. *Symp. (Int.) Combust.* **1994**, *25*, 901.